International Journal of Plasticity 174 (2024) 103919

Contents lists available at ScienceDirect

International Journal of Plasticity

journal homepage: www.elsevier.com/locate/ijplas

Short-range ordering mechanics in FCC materials

Daegun You [a], Orcun Koray Celebi [a], Gorkem Gengor [a], Ahmed Sameer Khan Mohammed [a], Wael Abuzaid [b], Huseyin Sehitoglu [a,*]

[a] Department of Mechanical Science and Engineering, University of Illinois at Urbana-Champaign, 1206W. Green St., Urbana, IL 61801, USA
[b] Department of Mechanical Engineering, American University of Sharjah, PO Box 26666, Sharjah, United Arab Emirates

ARTICLE INFO

Keywords:
Short-range order
Stacking fault
Critical stress
Dislocations
Wigner-seitz cell

ABSTRACT

Short-range order (SRO) has a crucial impact on the mechanical strength of metallic alloys. Recent atomistic investigations defined an average SRO and attempted to correlate it with the yield strength. We propose that the local change in SRO upon slip advance must dictate the strengthening, and we elaborate the methodology to establish the "SRO change" on a slip plane considering the Wigner-Seitz cell. The model captures the variation of lattice resistance (Critical Resolved Shear Stress; CRSS) in the crystal as the SRO changes depending on the probability of neighboring atoms. The methodology was applied to Ni-V binary alloys for a wide range of compositions and stacking fault widths. Dislocation core widths were determined as a function of SRO and energy parameters (unstable and intrinsic stacking fault energies; γ_{us}, γ_{isf}). The complex variation of CRSS with compositional variations shows good agreement with limited experimental results. The compositions corresponding to the transition from partial to full dislocations at higher vanadium contents are found depending on the SRO and the intrinsic energy levels.

1. Introduction

Short-range order (SRO) in crystalline alloys refers to the preferential positions that solute atoms occupy around a reference atom. It is defined upon consideration of series of shells surrounding the reference atom, so a large number of SRO values can be generated depending on the size of the cell considered. Typically, average SRO quantities over a domain are reported which can also be measured with diffuse scattering studies although local arrangements responsible for "SRO changes" upon atomic displacements are difficult to obtain experimentally. A comprehensive methodology based on atomistic simulations addressing the determination of SRO and its change upon slip deformation is the subject of this paper.

The SRO is expected to have significant impacts on mechanical properties, including the strengths and deformation behaviors of substitutional alloys (Chen et al., 2021a, 2021b; Li et al., 2019; Zhang et al., 2022, 2019; Zhou et al., 2022). In equiatomic NiCoCr ternary alloy, for instance, it is found that yield strength increases with aging (Zhang et al., 2020) upon achieving a higher SRO compared to the solution-treated condition. Also, along with strength enhancement, NiCoCr represents a large variation of stacking fault width (SFW) in the negative stacking fault energy (SFE) (Ding et al., 2018; Niu et al., 2018; You et al., 2023a; Zhao et al., 2019, 2017), statistically expected to result from the SRO arranged by multi-elements. A recent study, however, found that a simple binary $Ni_{63.2}V_{36.8}$ alloy has a higher yield strength compared to NiCoCr as well as the well-known high-entropy alloy NiCoCrFeMn (Oh et al., 2019). Although there is an explanation on vanadium solute considering only solid-solution hardening effect (Yin et al., 2020a), the

* Corresponding author.
E-mail address: huseyin@illinois.edu (H. Sehitoglu).

https://doi.org/10.1016/j.ijplas.2024.103919
Received 6 November 2023; Received in revised form 20 January 2024;
Available online 13 February 2024

SRO effect on strengthening and stacking fault (SF) is missing upon solute concentration and also underestimated in binary alloys. The addition of a secondary element vanadium to nickel could produce a number of compositions to illustrate the role of SRO which is considered in this study.

The definition of SRO in multi-component alloys has been established based on the Warren-Cowley (WC) formalism (Cowley, 1960; Norman and Warren, 2004). It involves determining a set of probabilities of finding a particular type of solute atom in a specific coordination shell around the central reference atom. In the case of random distribution, the SRO is ideally zero, and either if atoms of the same type dominate the shell over a random case SRO > 0, or if atoms of the different type dominate then SRO < 0. A key development has been made by Fine and Cohen on the change of SRO on the slip plane (Cohen and Fine, 1962). Albeit it simplified to capture the change of SRO, it did not consider the actual change of coordination in the shell, i.e., missing the breaking and restoring of bonds during a slip. In this study, we extend this key to analyze the "SRO change" on the Wigner-Seitz (WS) cell which provides a correct representation.

Although the early experimental observations referred to average SRO definitions over macroscopic domains, the motion of plane defect modifies the local SRO on each different slip-plane and the choice of the primitive cell is critical in evaluation of the SRO change. In this paper, we undertake local SRO calculations focusing on finite number of atoms governed by the WS cell. Such a treatment leads to the correct determination of the critical resolved shear stress (CRSS) as we will demonstrate.

Previous reports that mainly focused on the SRO obtained the WC-based SRO parameters via Monte Carlo (MC) simulations of swapping atomic species (Chen et al., 2021a; Ding et al., 2018; Tamm et al., 2015). The importance of SRO is gaining attention in both theoretical and experimental studies (Ferrari et al., 2023; Kostiuchenko et al., 2020; Picak et al., 2023; Singh et al., 2015; Ziehl et al., 2023). The MC approach has been well accepted. However, a rigorous treatment relating the SFE to the "SRO change" over the accurate cell-grid (WS cell in this work) is missing. Also, the variations in the SFEs and the SRO changes upon slip depend on each slip-plane, so a range of CRSS in the material can be correspondingly achieved with different slip-planes, which is consistent with experimental measurements. Therefore, with accurate formulation of the SRO change and its relation to SFE, one can potentially reduce the density functional theory (DFT) calculations to obtain thousands of SFEs representative of real materials.

In the given crystal with more than two elements, the variations of SFEs due to the different slip-planes correspond to the distinctive CRSS, since it is strongly dictated by the SFEs (Celebi et al., 2022, 2023; You et al., 2023a, 2023b). With a distribution of SFE or SFW, one can also obtain a range of dislocation core-widths based on the current theory we describe. Therefore, the dislocation core-width is not a constant value and varies depending on the local composition and the SRO. Hence, the determination of "SRO change" upon slip governs the SFEs hence the CRSS in different slip-planes.

In this study, we determine the variation of SRO during slip motion over the different slip-planes of FCC materials. We implement hybrid MC molecular dynamics (MD) simulations of swapping atomic species in FCC Ni-V binary alloys. For different bulk SRO states (average SRO of superlattice) of alloys, we apply a slip at a different slip-plane, and calculate the unstable and intrinsic SFEs, γ_{us} and γ_{isf}, based on DFT. We also calculate the average lattice constant and elastic constants (C_{11}, C_{12}, and C_{44}) for the model alloy system. Then, we evaluate the CRSS, SFW, and core-widths using the WS cell-based ab-initio framework by Mohammed-Celebi-Sehitoglu (MCS) (Celebi et al., 2023; Mohammed et al., 2022). By evaluating the variation of SRO with hundreds of slip-planes, we gain a more comprehensive understanding of the role of chemical SRO mechanics. By incorporating the interaction energy of atomic pairs into the SRO change, we show that the SFEs in different slip-planes can be predicted obviating the need for SFE simulations. We also reveal the effect of solute concentration on SFEs and CRSS, as well as core-widths and SFWs is rather complex. This work shows the capabilities of exact "SRO change" in determination of SFEs and CRSS and can guide the experiments.

An important distinction between this work and previous studies is the treatment of the "SRO change" upon slip. Upon slip displacements of magnitude $b/2$ and b within the WS lattice, where b is the magnitude of Burgers vector, certain bond pairs are lost while other pairs are added to the lattice. The atoms of pairs being lost and added can be different types of elements. This implies that the composition of the WS lattice is changing due to slip. Because different types of atoms are being introduced and removed, the local arrangement of atoms (i.e., SRO) also changes. In fact, the SRO is likely to decrease upon slip and the lattice structure becomes more random. This randomness is associated with a higher energy, similar to what is known as intrinsic faults within the lattice. Quantifying this change in SRO is a departure from previous studies, suggesting that understanding these changes could lead to an advanced treatment of CRSS in multi-component alloys.

Finally, in this study a further insight on finite temperature effects on the CRSS is presented by considering combined ab-initio MD (AIMD) simulations. This approach has not been undertaken previously to evaluate CRSS based on our knowledge. The DFT is utilized for the calculation of forces based on electronic structure calculations while the MD provides the solution for the classical equations of motion to capture the actual dynamics and the new positions of the nuclei. Convergence to the desired temperature in the range 0–700 K was achieved. Although computationally demanding, the method allows study of finite temperature effects and comparison of theory with experiments. The CRSS measurements in experiments are often conducted at room temperature and at 77 K (Abuzaid and Sehitoglu, 2017; Chowdhury et al., 2015; Liu et al., 2023). However, the DFT results are predominantly obtained at 0 K. Previous treatments of temperature effects in materials science have been semi-empirical and followed the developments from Ashby-Argon-Kocks-Haasen. However, these early treatments do not rely on first-principles calculations including electronic effects or the SRO effects considered in this work. The current treatment in this paper overcomes previous limitations and compares CRSS theory to experiments at finite temperatures as presented in the Appendix.

2. Methods

2.1. Hybrid Monte Carlo molecular dynamics of swapping atom

In order to get multiple SRO structures, we implement hybrid MC/MD simulations of swapping atomic species, each step performs DFT-based calculation. The hybrid MC/MD is suitable for the fast relaxation of crystal including atomic swaps with available interatomic potentials (Widom et al., 2014). In order to degrade empiricism in the potentials, we cross-validate energetics of atomic structures at each swapping atomic species using DFT via Vienna Ab-initio Simulation Package (VASP) (Kresse and Furthmüller, 1996). For hybrid MC/MD simulations of swapping atomic species, we utilize modified embedded atom model (MEAM) Ni-V interatomic potential (Shim et al., 2013), using the large-scale atomic/molecular massively parallel simulator (LAMMPS) package (Thompson et al., 2022). We create an oriented FCC Ni superlattice containing 270 atoms with 9 stacking layers of {111} plane. For targeting composition ratio, Ni atoms are correspondingly substituted to V atoms. Then, the hybrid MC/MD simulation of swapping atomic species (Ni and V) is carried out based on Metropolis-Hasting criterion (Hastings, 1970). It accepts the swapped configuration (1) if the energy of swapped configuration $E(i+1)$ is lower than the previous one $E(i)$, or (2) the following probability is equal to / greater than the random number (R) ranged by (0, 1),

$$R \leq \exp\left(-\frac{E(i+1)-E(i)}{kT_s}\right) \tag{1}$$

where k is Boltzmann constant, and T_s is temperature-scaling factor. We set it to 10 K for most compositions, except two more configurations (300 K, 500 K) in $Ni_{63.7}V_{36.3}$ composition for a structural variety. We apply 10 swapping atomic species in Ni and V at each MC step.

2.2. Short-range order characterization

For each hybrid MC/MD step, we calculate the DFT based energy and the Warren-Cowley (WC) based SRO parameters. The SRO

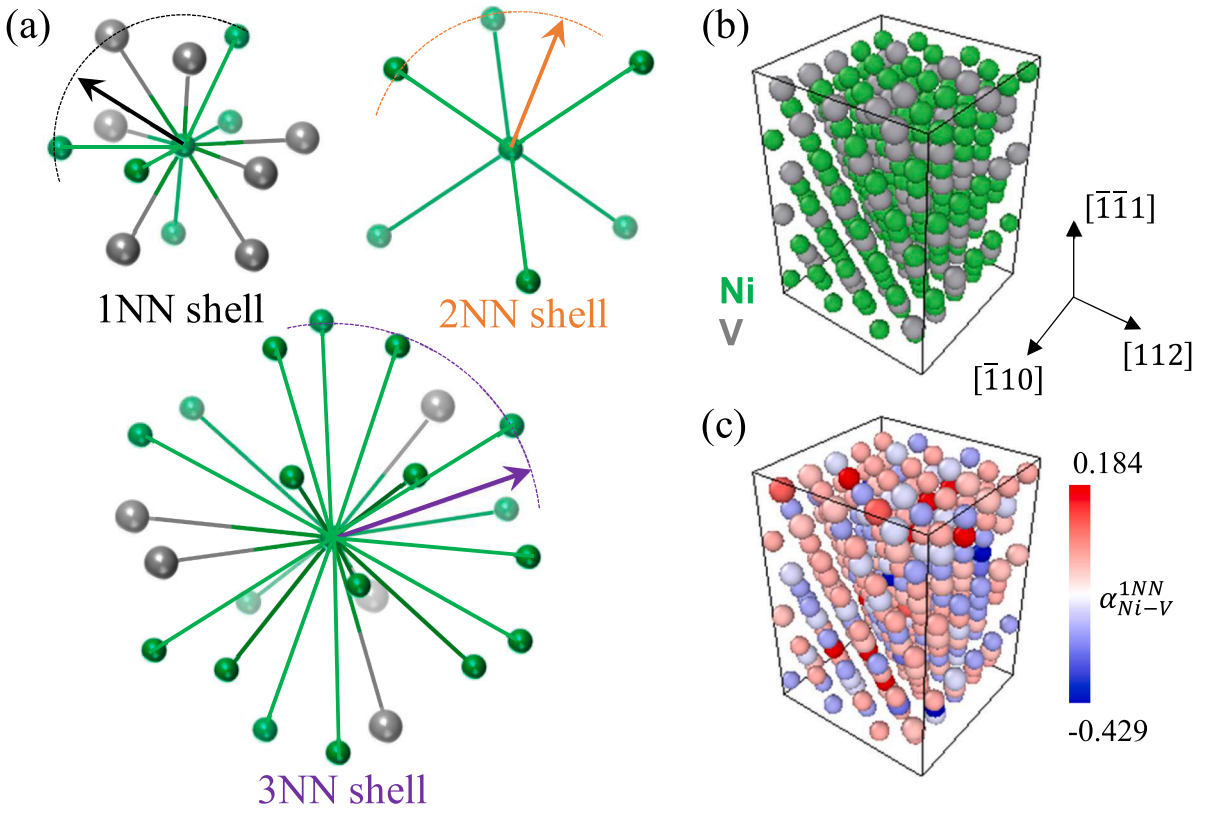

Fig. 1. Definition and illustration of short-range order (SRO). (a) Schematic of first, second, and third nearest-neighbor (NN) shells surrounding Ni center host atom in FCC binary Ni-V alloys; Ni and V atoms are colored green and grey, (b) Atomic configuration of FCC $Ni_{63.7}V_{36.3}$ alloy energetically converged in hybrid Monte Carlo (MC) molecular dynamics (MD) simulation; 270 atoms (Ni: 172, V: 98) within 9 {111} planes, (c) Warren-Cowley (WC) based SRO parameter (α_{i-j}^{m}) calculated in $Ni_{63.7}V_{36.3}$ alloy for the energetically converged superlattice.

parameters are defined at different nearest-neighbor (NN) shells surrounding the host atom. The SRO is defined as follows,

$$\alpha_{i-j}^{m} = 1 - \frac{p_{i-j}^{m}}{c_j} \tag{2}$$

where p_{i-j}^{m} is the probability of finding an atomic species (j) around the host (i) in m-th NN shell, and c_j is the concentration of an atomic species (j). In Fig. 1a, we illustrate three different NN shells in Ni-V binary alloys. In the Supplementary Materials, we plot the DFT based energy and the SRO parameters at three different NN shells in Fig. S1 for 10 K T_s-factor in hybrid MC/MD. It generally leads to the convergences of the energy as well as the SRO parameters calculated in three distinctive shells. In the main text, we focus on the SRO parameter for the first ($m = 1$) NN shell since it dominantly contributes to the SRO (see Appendix F). In Fig. 1b and c, we demonstrate the atomic configuration and the SRO distribution of FCC $Ni_{63.7}V_{36.3}$ alloy (Ni: 172, V: 98) energetically converged in the hybrid MC/MD simulation. We obtain 12 different bulk SRO states (including randomly shuffled, special quasi-random; SQS, 7 intermediates, and three final structures using different T_s-factors) of $Ni_{63.7}V_{36.3}$, and 2 states (SQS, and final) of other compositions (5, 10, 15, 20, 25, and 30 at.%). For constructing SQS structure, we utilize ATAT package (van de Walle et al., 2013) to get the structure of the closest to zero SRO, i.e., the most random.

2.3. Density functional theory calculation

For different bulk SRO states of Ni-V alloys, we calculate the average lattice constant and elastic constants (C_{11}, C_{12}, and C_{44}) for the superlattice based on the DFT calculation. We use volumetric-energy and strain-energy methods in determination of the lattice constant and elastic constants (C_{11}, C_{12}, and C_{44}). In the Supplementary Materials, we demonstrate the details of calculations. After optimizing the lattice constant, we apply a slip at a different atomic plane, and calculate the SFEs. The SFE curve is calculated as below,

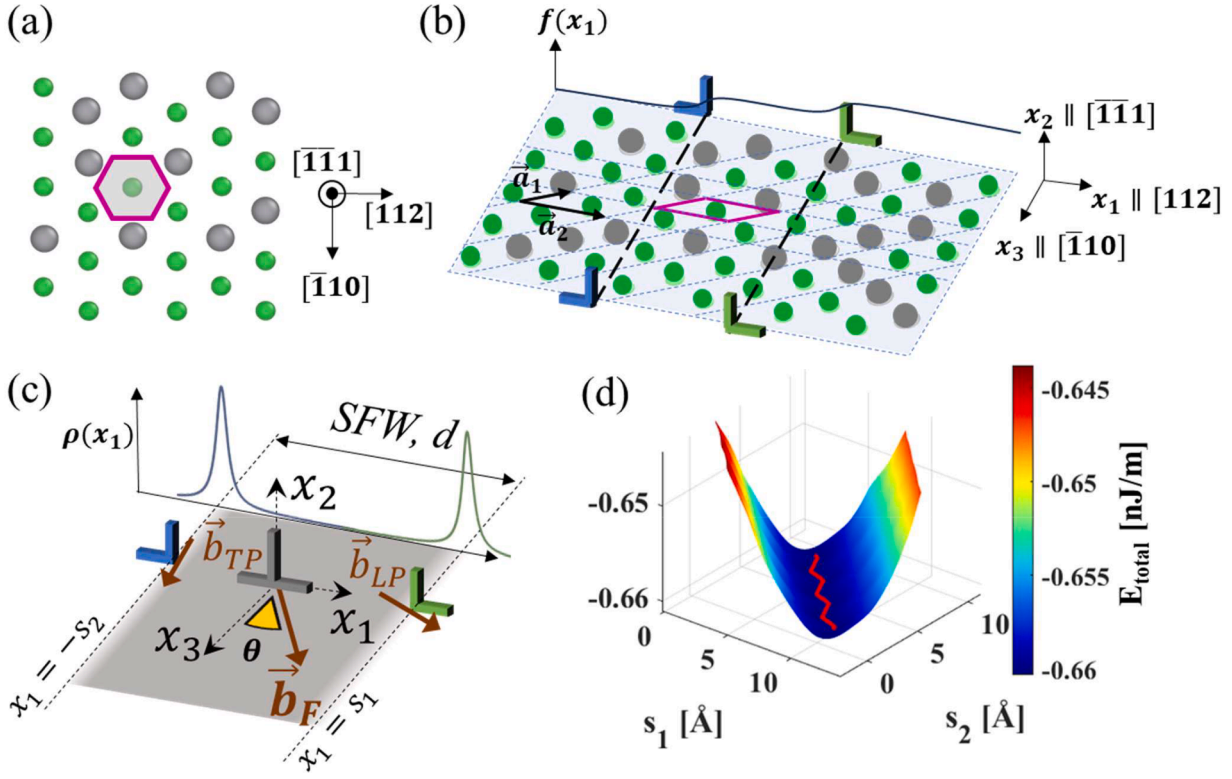

Fig. 2. Schematic of the extended dislocation and Wigner-Seitz (WS) cell-based misfit energy and CRSS framework; (a) the conventional WS cell area defined in {111} plane; Ni and V atoms are colored green and grey. (b) Atomic structure in {111} plane of $Ni_{63.7}V_{36.3}$ alloy equally spaced by the alternative WS cell area aligned with lattice vectors; Disregistry distribution function $f(x_1)$ is plotted. (c) For a given core-structure of an extended dislocation in FCC materials with full Burgers vector ($\vec{b}_F$), $\vec{b}_{LP}$ is the one for a leading partial, and $\vec{b}_{TP}$ for a trailing partial. $\vec{b}_F$ can be pure screw, edge, or mixed dislocation with angle of θ; Two Shockley partials are separated by stacking fault width (SFW, d); The LP is at position $x_1 = s_1$ and the TP is at $x_1 = -s_2$, yielding the SFW as a distance between two partials, $d = s_1 + s_2$; Two partials have elastically anisotropic interaction with each other, and atomistic misfit occurs in a slip-plane lattice; Dislocation-density distribution $\rho(x_1)$ is plotted with the core-widths ξ_{TP}, ξ_{LP} of the trailing and leading partials, respectively; (d) Typical total energy contour determined by the WS cell-based framework for $Ni_{63.7}V_{36.3}$ alloy; Screw dislocation is considered in this sample.

suggested by Vítek (1968),

$$\gamma = \frac{E - E_0}{A} \tag{3}$$

where E_0 and E are energies of initial and deformed states, and A is an area of slip-plane. The DFT calculations are implemented within the projected-augmented-waves (PAW) (Kresse and Joubert, 1999) approach via Perdew-Burke-Ernzerhof (PBE) (Perdew et al., 1996) exchange-correlation potentials. The PAW-PBE pseudopotentials for V and Ni are employed with V_sv and Ni_pv, respectively. The oriented FCC superlattice with 270 atoms is employed with Monkhorst-pack k-mesh $1 \times 1 \times 1$ for hybrid MC/MD swapping atoms, $2 \times 2 \times 2$ for electronic minimization and ionic relaxation in allowing full distortions, lattice volumetric optimization, and elastic constants, and $2 \times 2 \times 1$ for determining SFEs to hinder redundant SFs outside the periodic boundary. A 450 eV plane-wave energy cut-off is used for all the calculations. The tolerance criteria for energy and force are allowed within 1 meV and 5 meV/Å, respectively. For finite temperature simulations in AIMD, we use the same structures firstly optimized at 0 K. Details of AIMD are summarized in Appendix A.

2.4. Wigner-Seitz cell based analytic framework

The CRSS analytical framework is based on the notion of energy minimization utilizing a WS cell-based cell on the slip plane to establish the dislocation core width and partial dislocation separation. Fig. 2 represents the typical schematic and results based on the previous framework suggested by Mohammed-Celebi-Sehitoglu (abbreviated as MCS) (Mohammed et al., 2022). It has the originality of combining the anisotropic elastic interaction, the WS cell-based atomistic misfit energy, and the energy-minimization of intermittent motion of Shockley partial dislocations in FCC materials. In Fig. 2a, the conventional WS cell area is represented as purple hexagon in the atomic structure of {111} plane schematic in $Ni_{63.7}V_{36.3}$ alloy. This original definition of the WS cell is kept for later SRO calculation. In Fig. 2b, the equivalent WS cell area aligned with lattice vectors in {111} plane. This alternative WS cell area is proper to characterize the CRSS incorporated with the SFEs. Also, the core-disregistry distribution function $f(x_1)$ is plotted against slip-direction.

In Fig. 2c, the core structure of an extended dislocation is depicted. As a slip occurs, the separated partials have a repulsive elastic interaction. At the same time, the WS cell-based misfit energy in a crystal lattice produces an attractive force and balances the elastic component. The total energy is a minimum at a finite separation distance. Also, the full, leading, and trailing partial Burgers vectors ($\vec{b}_F$, $\vec{b}_{LP}$, and $\vec{b}_{TP}$) are represented. A dislocation character, the angle between $\vec{b}_F$ and the dislocation line, can result from various vectors in the specific coordinate system. Alternatively, we consider the fixed Burgers vectors as the references of the extended dislocation and vary the global coordinate systems. In this work, we demonstrate the framework mainly based on a screw dislocation with different SRO states and slip-planes in $Ni_{63.7}V_{36.3}$ alloy. The macroscopic material constants such as lattice constant and elastic constants C_{11}, C_{12}, C_{44} are considered for different SRO states, while the unstable and intrinsic stacking fault energies γ_{us} and γ_{isf} are for different slip-planes. The global coordinate for the screw character is defined as $\vec{e}_1 \| [1\bar{1}2]$, $\vec{e}_2 \| [1\bar{1}1]$, and $\vec{e}_3 \| [\bar{1}\bar{1}0]$.

The dislocation-density distribution $\rho(x_1)$ is plotted in Fig. 2c. As a slip is introduced, the density of a full dislocation becomes separated into two components for Shockley partials, including the leading (LP) and trailing partials (TP) with the core-widths ξ_{LP} and ξ_{TP}, respectively. A distance between two partials is then characterized by the SFW as d. The distributions are derived from the core disregistry functions, $f(x_1)$, of the LP and TP. Both the core-disregistry distributions $f(x_1)$ and dislocation-density distributions $\rho(x_1)$ for the partial Burgers vectors are defined as the following equations

$$f_{LP}(x_1) = \frac{b_p}{2} + \frac{b_p}{\pi}\tan^{-1}\left(\frac{x_1 - s_1}{\xi_{LP}}\right);\ \rho_{LP}(x_1) = \frac{b_P}{\pi}\left(\frac{\xi_{LP}}{(x_1 - s_1)^2 + \xi_{LP}^2}\right) \tag{4}$$

$$f_{TP}(x_1) = \frac{b_p}{2} + \frac{b_p}{\pi}\tan^{-1}\left(\frac{x_1 + s_2}{\xi_{TP}}\right);\ \rho_{TP}(x_1) = \frac{b_P}{\pi}\left(\frac{\xi_{TP}}{(x_1 + s_2)^2 + \xi_{TP}^2}\right) \tag{5}$$

where b_p is the magnitude of the partial Burgers vector, and s_1, s_2 are the positions of LP and TP respectively, which determines the SFW as $d = s_1 + s_2$. Eqs. (4) and (5) are established in dislocation core model with respect to two Shockley partials where $f(x_1)$ is distance registry across the slip plane following arctan function and $\rho(x_1)$ is derivative of $f(x_1)$. These explicitly represent the several key parameters of the core structures in the extended dislocation, such as the core-width ξ_{LP}, ξ_{TP}, and the SFW based on the positions of partials. In the previous studies on the MCS framework, the core structure parameters are determined upon minimization of total energy (E_{total}) of the extended dislocation in FCC crystals, as E_{total} is composed of two energy components,

$$E_{total}(\xi_{LP}, \xi_{TP},\ s_1, s_2) = E_{strain}(\xi_{LP}, \xi_{TP},\ s_1, s_2) + E_{misfit}(\xi_{LP}, \xi_{TP},\ s_1, s_2) \tag{6}$$

where E_{strain} is the elastic strain energy based on the anisotropic Eshelby-Stroh (E-S) formalism (Barnett and Lothe, 1974; Stroh, 1958), and E_{misfit} is the misfit energy utilizing the equivalent WS cell area in the crystal lattice. For the details of the elastic strain-energy and misfit energy formalism, the reader may refer to elsewhere (Mohammed et al., 2022).

The strain energy component $E_{strain}(\xi_{LP}, \xi_{TP},\ s_1, s_2)$ for the extended dislocation can be calculated from the anisotropic interaction coefficients on each Shockley partial. $E_{strain}(\xi_{LP}, \xi_{TP},\ s_1, s_2)$ consists of the self-interaction energies of the LP and TP (such as $E^{11}_{elastic}$ and

$E^{22}_{elastic}$, respectively) and the interaction energy between the two partials ($E^{12}_{elastic}$). Therefore, $E_{strain}(\xi_{LP}, \xi_{TP}, s_1, s_2)$ is expressed as

$$E_{strain}(\xi_{LP}, \xi_{TP}, s_1, s_2) = E^{11}_{elastic} + E^{22}_{elastic} + E^{12}_{elastic} \tag{7}$$

All terms on the right-hand side are summed up with the elastic interaction energy between infinitesimal fractional dislocations derived from the cores of the partials, and they are defined as follow,

$$\begin{aligned} E^{11}_{elastic} &= \int_{-\infty}^{\infty}\int_{-\infty}^{\infty}\left(\frac{K_{11}}{2\pi}\right)\rho_{LP}(x)\rho_{LP}(y)\ln|x-y|dxdy \\ E^{22}_{elastic} &= \int_{-\infty}^{\infty}\int_{-\infty}^{\infty}\left(\frac{K_{22}}{2\pi}\right)\rho_{TP}(x)\rho_{TP}(y)\ln|x-y|dxdy \\ E^{12}_{elastic} &= \int_{-\infty}^{\infty}\int_{-\infty}^{\infty}\left(\frac{K_{12}}{2\pi}\right)\rho_{LP}(x)\rho_{TP}(y)\left(\vec{b}_{LP}.\vec{b}_{TP}\right)\ln|x-y|dxdy \end{aligned} \tag{8}$$

where K_{11}, K_{22}, and K_{12} are the anisotropic interaction coefficients to be computed. As an example, the procedure to determine K_{12} can be briefly explained. We can consider the LP and TP separated by a certain distance R. The continuum strain-fields surrounding each Shockley partial are determined and superposed based on the E-S formalism to determine the net strain-field. The strain energy density is then numerically integrated to calculate the total strain-energy of interaction at the chosen separation distance R, and a core region within radius $5b_p$ around the center of each partial is excluded. By calculating the total strain-energy at varying R, the interaction coefficient K_{12} is determined. The choice of $5b_p$ does not affect K_{12} calculation since the gradient of change of total strain-energy is conserved. The self-interaction coefficients K_{11} and K_{22} can be similarly determined by considering the interaction between two dislocations with the same Burgers vectors of them. For a more detailed exposition of anisotropic interaction coefficients and the E-S formalism, the reader is referred to elsewhere (Mohammed et al., 2022).

For the formulation of the WS cell-based misfit energy $E_{misfit}(\xi_{LP}, \xi_{TP}, s_1, s_2)$, the generalized stacking fault energy (GSFE) curve is required for each LP and TP. The GSFE curves for the LP and TP are defined as:

$$\gamma_{LP}(u) = \begin{cases} \gamma_{isf} + \left(\frac{\gamma_{us}-\gamma_{isf}}{2}\right)\left(1-\cos\left(\frac{2\pi u}{b_P}\right)\right) & \text{for } 0 \le u \le \frac{b_P}{2} \\ \frac{\gamma_{us}}{2}\left(1-\cos\left(\frac{2\pi u}{b_P}\right)\right) & \text{for } \frac{b_P}{2} \le u \le b_P \end{cases} \tag{9}$$

$$\gamma_{TP}(u) = \begin{cases} \frac{\gamma_{us}}{2}\left(1-\cos\left(\frac{2\pi u}{b_P}\right)\right) & \text{for } 0 \le u \le \frac{b_P}{2} \\ \gamma_{isf} + \left(\frac{\gamma_{us}-\gamma_{isf}}{2}\right)\left(1-\cos\left(\frac{2\pi u}{b_P}\right)\right) & \text{for } \frac{b_P}{2} \le u \le b_P \end{cases} \tag{10}$$

where γ_{us} and γ_{isf} are unstable and intrinsic stacking fault energies, respectively. Eqs. (9) and (10) are established by Fourier series with two critical energy barriers γ_{us} and γ_{isf}. The reader is referred to elsewhere (Kibey et al., 2006) for a more detailed exposition of GSFE curve. Based on Eqs. (4), (5), and (9), (10), the E_{misfit} can be rewritten with the partitioned GSFE into the WS cell area for the individual Shockley partials,

$$E_{misfit}(\xi_{LP}, \xi_{TP}, s_1, s_2) = \frac{1}{L_{2D}}\left[\begin{array}{l} \sum_{n=-N_0}^{N_0}\sum_{m=-M_{max}}^{-1}\gamma_{TP}\left(f_{TP}\left(x_1^{(m,n)}\right)\right)\Delta A \\ \ldots\ldots + \sum_{n=-N_0}^{N_0}\sum_{m=0}^{M_{max}}\gamma_{LP}\left(f_{LP}\left(x_1^{(m,n)}\right)\right)\Delta A \end{array}\right] \tag{11}$$

where $x_1^{(m,n)} = (m\vec{a}_1 + n\vec{a}_2)\cdot\vec{e}_1$, ΔA is the area of the WS cell, and L_{2D} is the normalization length in the repeated dislocation lines. A summation limit of M_{max} is chosen with a large number, of the order of 10^4, to sufficiently converge the $E_{misfit}(\xi_{LP}, \xi_{TP}, s_1, s_2)$. The misfit energy in Eq. (11) is calculated per unit length of the dislocation line. For the positive γ_{isf}, four parameters $(\xi_{LP}, \xi_{TP}, s_1, s_2)$ are consequently determined by the Eq. (6) with respect to the equilibrium core structure $(\xi^0_{LP}, \xi^0_{TP}, s^0_1, s^0_2)$ at the global minimum of E_{total} in such that

$$\frac{\partial E_{total}}{\partial \xi_{LP}} = 0;\ \frac{\partial E_{total}}{\partial \xi_{TP}} = 0;\ \frac{\partial E_{total}}{\partial s_1} = 0;\ \frac{\partial E_{total}}{\partial s_2} = 0 \tag{12}$$

The minimization routine is implemented with *fmincon* in MATLAB. Details for the dependence of each energy component on the core parameters are found in the previous study (Celebi et al., 2023; Mohammed et al., 2022).

2.5. Minimum energy path (MEP) of partial dislocations and crss

The previous MCS framework formulated the minimum energy path (MEP) with the equilibrium core-widths ($\xi^0_{LP},\ \xi^0_{TP}$) to find the triangular trajectory that allows the robust intermittent movement of Shockley partials (Mohammed et al., 2022; You et al., 2023b), which is also energetically favorable than the constant dissociation of partials. The positions of Shockley partials (s_1, s_2) are described by the following equations along with the triangular trajectory,

$$\begin{aligned} s_1 &= s_1^0 + \frac{1}{\sqrt{2}}\left(t + \sum_{k=1}^{n} C_k\left(1 - P\left(C_p, j\right)\right)\right) \\ s_2 &= s_2^0 + \frac{1}{\sqrt{2}}\left(-t + \sum_{k=1}^{n} C_k\left(1 - P\left(C_p, j\right)\right)\right) \end{aligned} \tag{13}$$

where t is a path variable to parametrize the trajectory. $P(C_p, j)$ is the triangular pulse generator and j is a pulse-variable defined as follows,

$$j = \frac{t}{C_q} + C_p - \left\lfloor \frac{t}{C_q} + C_p \right\rfloor \tag{14}$$

$$P\left(C_p, j\right) = \begin{cases} 0 & \text{for } j \le 0 \\ \dfrac{j}{C_p} & \text{for } 0 < j < C_p \\ \dfrac{1-j}{1-C_p} & \text{for } C_p < j < 1 \\ 0 & \text{for } j \ge 1 \end{cases} \tag{15}$$

where the lower bracket of $\lfloor x \rfloor$ is a floor function $\lfloor x \rfloor . = \max\{X \in \mathbb{Z} : X \le x\}$, and the parameter combination $(C_1, \ldots, C_n, C_p, C_q)$ defines a shape for a triangular path of positions of Shockley partials. The total energy cumulated along with the triangular trajectory given in Eq. (13) is accordingly defined as the following objective function,

$$E_{path}\left(C_1, \ldots, C_n, C_p, C_q\right) = \sum_i E_{total}\left(s_1(t_i), s_2(t_i), \xi^0_{LP},\ \xi^0_{TP}\right) \tag{16}$$

Eq. (13) and (16) respectively describe the triangular trajectories and energy landscape based on the positions of two Shockley partials corresponding to the minimum energy path, which were established in the previous papers (Mohammed et al., 2022; You et al., 2023b). The number of periodic functions is simply set to $n = 1$ sufficient to capture the MEP. The roles of path parameters such as t and (C_1, C_p, C_q) can be also understood with the equilibrium point found at $t = 0$ for (s_1^0, s_2^0) and the positive γ_{isf} with $C_1 = 0$, which is the amplitude of triangular path. C_p and C_q are a peak position and a period of the triangular path, respectively. The triangular pulse generator $P(C_p, j)$ is implemented with *triangularPulse* in MATLAB. The equilibrium parameters $(\xi^0_{LP},\ \xi^0_{TP}, s_1^0, s_2^0)$ for the case of positive γ_{isf} are employed along with the triangular trajectory described by Eq. (13), and the minimization routine in Eq. (16) is also implemented with *fmincon* and multiple initial points (*MultiStart*) in MATLAB to find the corresponding MEP.

In the conventional Peierls-Nabarro (PN) model (Joós and Duesbery, 1997; Nabarro, 1947; Peierls, 1940), the CRSS has been calculated by taking only the simple misfit energy based on the one-dimensional cubic row-summation. Thus, it is expressed as,

$$CRSS_{PN} = \max\left(\frac{1}{b_F}\frac{dE^{PN}_{misfit}}{du}\right) \tag{17}$$

where b_F is the magnitude of the full dislocation, $E^{PN}_{misfit}(u) = \sum_{m=-\infty}^{\infty}\gamma(f(ma' - u))a'$, γ is the GSFE curve, f is the disregistry function given by equation x, and a' is interplanar spacing perpendicular to the dislocation line, respectively. The MCS framework suggested the optimum-energy-trajectory (OET) approach for the CRSS prediction that resolved the limitations in the PN model such as (i) the motion of individual Shockley partials with a constant SFW, (ii) the dependency of CRSS on the full Burgers vector b_F only, not on the partial Burgers vector b_p, and (iii) the one-dimensional simple-cubic row-summation misfit-energy. For more detailed coverage of the OET approach and its derivation, readers are referred to the original work (Mohammed et al., 2022). Based on the OET approach, the CRSS is defined as,

$$CRSS_{MCS} = SF_F \cdot \max\left(\frac{1}{\left(SF_{LP} \cdot s_1'(t) - SF_{TP} \cdot s_2'(t)\right)}\frac{1}{b_p}\frac{dE_{total}}{dt}\right) \tag{18}$$

where b_p is the magnitude of the Burgers vector in Shockley partials, $SF_F = (\vec{\nu} \cdot \vec{n}_{slip})(\vec{\nu} \cdot \vec{b}_F)$, $SF_{LP} = (\vec{\nu} \cdot \vec{n}_{slip})(\vec{\nu} \cdot \vec{b}_{LP})$, and $SF_{TP} = (\vec{\nu} \cdot \vec{n}_{slip})(\vec{\nu} \cdot \vec{b}_{TP})$ are Schmid Factors (SFs) resolved in the full extended dislocation, LP, and TP, $\vec{\nu}$ is the unit vector along the uniaxial

tensile load direction $[1\bar{3}2]$, and $\vec{n}_{slip} = 1/\sqrt{3}[1\bar{1}1]$ the normal vector to the slip plane, respectively. The CRSS in Eq. (18) appears different than the conventional PN approach in Eq. (17) where a single partial is solely considered, since the OET approach in this work includes partial separation trajectory.

In Fig. 2d, a typical result for $Ni_{63.7}V_{36.3}$ alloy is shown with the MCS framework for a screw dislocation. The material parameters are determined by DFT calculation such as $a = 3.597$ Å, $C_{11} = 265.2$ GPa, $C_{12} = 177.4$ GPa, $C_{44} = 122.2$ GPa, $\gamma_{us} = 277.0$ mJ/m^2, and $\gamma_{isf} = 85.7$ mJ/m^2. This parameter-set is one of data in $Ni_{63.7}V_{36.3}$ alloy which is covered in the next section. In the total energy contour along with the positions of Shockley partials (s_1, s_2), the optimized MEP (red line) is represented. Based on the minimization in Eq. (12), the equilibrium core widths (ξ^0_{LP}, ξ^0_{TP}) of Shockley partials yield both $\xi^0_{LP} = \xi^0_{TP} = 3.39$ Å, and their equilibrium positions (s^0_1,s^0_2) are (6.48 Å, 4.27 Å), which results in the global equilibrium SFW, $d_0 = 10.7$ Å. Then, the CRSS of the given input parameters finally yields the CRSS = 13.4 MPa based on Eq. (18), at the maximum derivative of total energy, which is resolved in its OET. The fluctuation in the SFW is due to the intermittent zig-zag motion of Shockley partials.

3. Results and discussion

3.1. Bulk and planar SRO in material constants

For the SRO characterization of the given crystal, the average over total number of atoms is generally used. The average SRO is defined as follows,

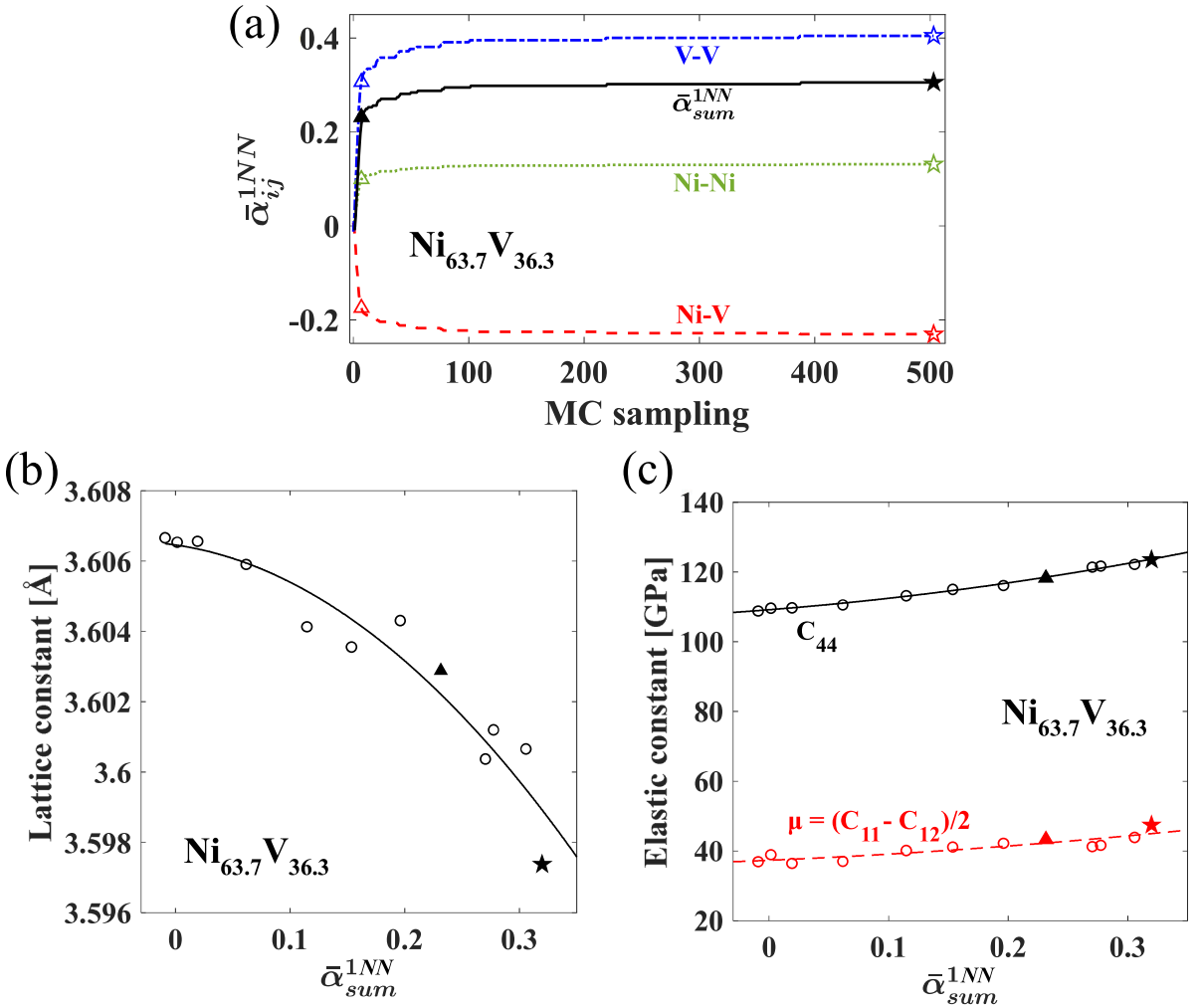

Fig. 3. Short-range order (SRO) effect in material bulk properties of $Ni_{63.7}V_{36.3}$ alloy; (a) an average of the WC-based SRO parameters over total number of atoms ($\bar{\alpha}^m_{i-j}$); intermediate (triangle) and final (asterisk) structures are denoted as examples; total 12 different atomistic structures are sampled, (b) averages of lattice constant and (c) elastic constants (C_{11}, C_{12}, C_{44}) as a function of summation of all pairs ($\bar{\alpha}^m_{sum}$) for 12 structures.

$$\bar{\alpha}^m_{i-j} = \frac{1}{n_{i-j}} \sum_{k=1}^{n_{i-j}} \alpha^m_{i-j,k} \tag{19}$$

where n_{i-j} is total number of atoms for $i-j$ pairs, and $\alpha^m_{i-j,k}$ is the SRO at k-th site of center atomic species i. For $Ni_{63.7}V_{36.3}$ alloy composition (Ni: 172, V: 98), we have 172 Ni-Ni pairs, 270 Ni-V pairs, and 98 V-V pairs, respectively. In Fig. 3a, the average SRO parameters $\bar{\alpha}^m_{i-j}$ for the first NN shell (1NN) in different types of pair are shown. The average quantities of pairs for the second and third NN shells are depicted in Fig. S1 in the Supplementary Materials. As $Ni_{63.7}V_{36.3}$ alloy is being energetically stabilized, the SRO is converged and Ni-V pair (-) becomes more favorable than Ni-Ni and V-V pairs (+) in the 1NN shell. We put the summation of each pair SRO parameter, defined as below,

$$\bar{\alpha}^m_{sum} = \sum_{pair} \sum_{i-j} \bar{\alpha}^m_{i-j} \tag{20}$$

We sampled out 12 different SRO states by using the average pair summation measurer. Two example structures are denoted by intermediate (triangle) and final (asterisk) ones. With 12 distinctive bulk SRO states, the lattice constant, and elastic constants (C_{11}, C_{12}, and C_{44}). are varying in Fig. 3b and c. The details of determination of these constants are given in Fig. S2 in the Supplementary Materials. Since these material parameters (lattice constant and elastic constants) are usually characterized in the macroscopic deformation of given supercell, the average SRO quantity for total number of atoms indicates a good correlation. As the alloy is stabilized with respect to the energy and SRO parameters, the lattice constant decreases while the elastic constants (μ, C_{44}) increase overall. This is because the lattice distortions decrease as the atomic configurations transition from a random configuration to a short-range ordered configuration. These changes may contribute to the CRSS increase or decrease for general FCC materials (You et al., 2023b). The decreases in lattice constant and elastic constants are correlated with the increase in the CRSS. However, the changes are small, and the opposite contribution caused by decreasing lattice constant and increasing elastic constants may lead counterbalance to the CRSS. Therefore, other material constants such as unstable and intrinsic SFEs (γ_{us}, γ_{isf}) are possibly critical factors to the CRSS, as we show in the next section.

In Fig. 4, we show a large variation of the SFEs in the different slip-planes by taking samples from the stabilized atomic configuration of $Ni_{63.7}V_{36.3}$ alloy in the hybrid MC/MD simulations at 10 K T_s-factor. We take three different slip-planes in the illustration shown in Fig. 4a, and they have heterogenous configurations in the slip-planes. Hence, it should be considered in the local definition of the SRO. We calculate the planar SRO parameters for three slip-planes. Each slip-plane is considered as the center atomic layer in the SRO calculation. In Fig. 4b, the SFE curves are shown for three slip-planes and the case of pure Ni as a comparer. It shows significant changes in SFE curves by selecting the different slip-planes, although they come from the same macroscopic SRO state. The unstable and intrinsic SFEs (γ_{us}, γ_{isf}) for slip-planes A, B, and C are respectively (277.0 mJ/m^2, 85.7 mJ/m^2), (273.8 mJ/m^2, 175.6 mJ/m^2), and

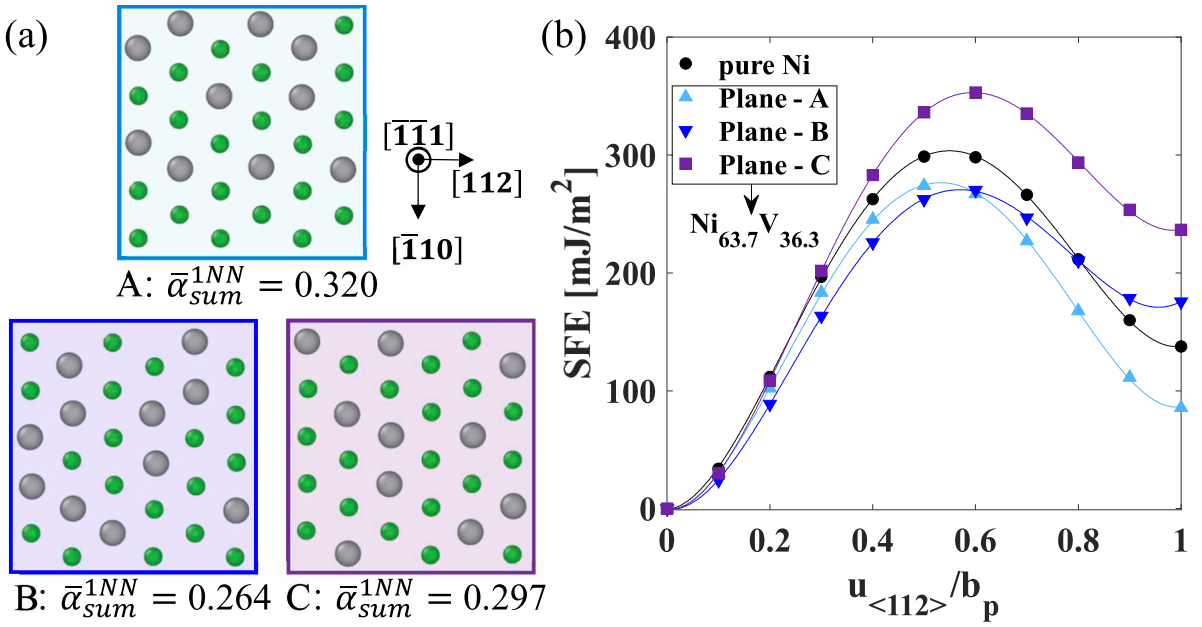

Fig. 4. Stacking fault energies (SFEs) with different slip-planes. (a) initial (before slip) states with varying slip-planes for the stabilized atomistic configuration of $Ni_{63.7}V_{36.3}$ alloy in hybrid MC/MD simulation; A, B, and C slip-planes are given as examples; Each planar SRO parameter is calculated by only considering each slip-plane as the center atomic layer; Ni and V atoms are colored green and grey. (b) SFEs upon slip displacement ($u_{\langle 112\rangle}$) from zero to intrinsic stacking fault (ISF) points; Selecting slip-planes significantly changes SFEs, even with the same macroscopic SRO state; SFEs for pure Ni is also given and compared; the Burgers vector is $\frac{a}{6}\langle 112\rangle$, where a is lattice constant.

(356.1 mJ/m^2, 236.5 mJ/m^2), while the one for pure Ni is (299.0 mJ/m^2, 137.6 mJ/m^2). The planar SROs in three slip-planes ($\bar{\alpha}^{1NN}_{sum}$; 0.32, 0.264, 0.297) are distinctive from each other, while these are not enough to explain their correlations with the SFEs (γ_{us}, γ_{isf}). As SFEs are varying upon slip displacement, the SROs in all atomic sites in each A, B, and C slip-plane are also changing during the slip motion. This has to be considered as well in the SRO characterization. In the next section, we formulate the "SRO change" upon slip, and investigate its contribution to the SFEs and the CRSS.

3.2. Planar "SRO change" upon slip in Wigner-Seitz lattice

In Fig. 5, we illustrate the change of SRO parameter during slip motion. We demonstrate the SRO change for a single Ni atom sampled from the superlattice of $Ni_{63.7}V_{36.3}$ alloy, and the 1NN shell is defined with the WS cell during the slip. In Fig. 5a, we illustrate it in 3D view with three layers for the 1NN including a center layer ($Layer_0$) and two layers ($Layer_{+1}$, $Layer_{-1}$). In the calculation of SRO parameter, the host Ni atom in $Layer_0$ is considered as the center atom. Two layers ($Layer_{+1}$, $Layer_{-1}$) are overlaid together as shown in Fig. 5b. The initial coordination number becomes 12, and the number of Ni-V pairs is 7. After the slip displacement around half of Burgers vector, the material reaches to the unstable stacking fault (USF) point with the energy barrier γ_{us} to overcome. Then the V atom in the initial 12th site of the $Layer_{-1}$ is outside the WS cell, and its bond to the center Ni is broken in the 1NN shell based on the WS cell definition. Then the coordination number and the number of Ni-V pairs are respectively changed to 11 and 6. This significantly contributes to the SRO value. Similarly, at the intrinsic stacking fault (ISF) states, the new Ni atom in $Layer_{-1}$ is included in the WS cell as new 12th site ('12'), so its bond to the center Ni is restored. The coordination number becomes 12 again but the number of Ni-V pairs is already changed at the USF, so all three states (initial, USF, ISF) have distinctive SRO values (−0.607, −0.503, −0.378).

This definition can be extended to different slip-planes by also applying local concentration of substitutional solute atoms. The concentration c_j in Eq. (2) can be substituted with the local compositions (such as $Layer_0$, $Layer_{(-1,0)}$, or $Layer_{(-1,0,+1)}$ composition). Then, the pair probability defined in the WS cell and the local composition in the slip-plane result in more accurate characterization of SRO parameters during slip motion. We also apply the current definition to the multiple WS cells in the slip-plane ($Layer_0$). A total of 30 WS cells (center atoms) in the slip-plane can be averaged into a single WS cell value with respect to each pair such as Ni-Ni, Ni-V, and V-V. Then we can analyze the correlation of accurate SRO metrics with the SFEs and CRSS.

Fig. 6 represents the change of WS cell-based SRO parameters upon slip motion and its correlation with the SFEs and CRSS. We use

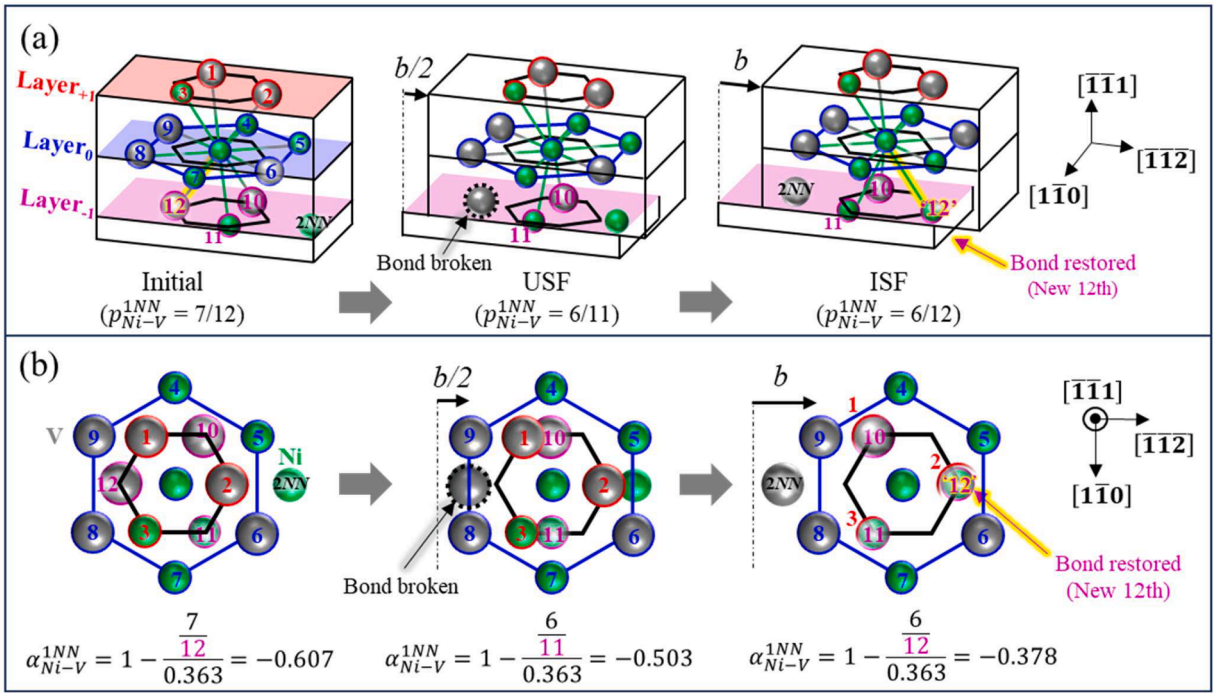

Fig. 5. Schematic of "short-range order (SRO) change" on a single host atom during slip motion; (a) Total 3-layers (color-surfaces / color-outlines of atoms) illustrate a center layer ($Layer_0$; blue) and two layers ($Layer_{+1}$, $Layer_{-1}$) upper and below $Layer_0$. Color-outlines of atoms correspond to their layer colors. $Layer_0$ is considered as the center atomic layer for calculating the SRO parameters upon slip throughout initial, unstable stacking fault (USF), and intrinsic stacking fault (ISF) states; For the Wigner-Seitz (WS) cell based planar SRO, an initial bond is broken around USF point, while a new bond is restored at ISF; Coordination number and probability (p^m_{i-j}) of Ni-V pair are changed upon slip for selected host atom; Ni and V atoms are colored green and grey; The WS cell is represented as black hexagon defined in center Ni atom. (b) In the {111} plane view, the change of SRO during slip motion is illustrated. The WS cell (black hexagon) is projected in the plane. $Layer_{+1}$ consists of atomic sites (1–3), $Layer_0$ (4–9), and $Layer_{-1}$ (10–12), respectively; By breaking or restoring the bond, the SRO α^m_{i-j} of Ni-V pair is changed.

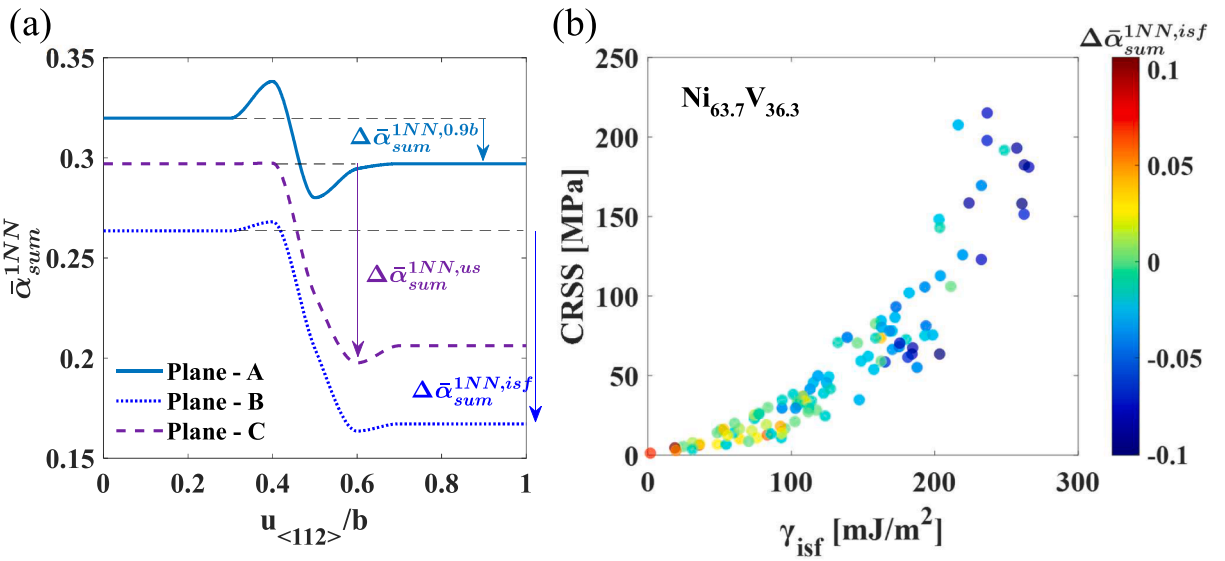

Fig. 6. Change of SRO based on the WS cell during slip motion; (a) $\bar{\alpha}_{sum}^{1NN}$ defined at slip-plane ($Layer_0$) varies upon slip deformation; Each slip-plane stems from Fig. 4 as a representation example; $\Delta\bar{\alpha}_{sum}^{1NN,u_{\langle 112\rangle}}$ is defined as the difference of $\bar{\alpha}_{sum}^{m}$ between $u_{\langle 112\rangle}$ distorted and initial states, (b) CRSS (screw) variation for intrinsic stacking fault energy (γ_{isf}) and $\Delta\bar{\alpha}_{sum}^{1NN,u_{\langle 112\rangle}}$ at ISF point with 9 different slip-planes in 12 different atomistic structures (total 108 data) of $Ni_{63.7}V_{36.3}$ alloy.

the average pair summation measurer $\bar{\alpha}_{sum}^{1NN}$ by using Eqs. (19) and (20) defined in the plane. The local composition, c_j, is based on two planes ($Layer_{(-1,0)}$) that contribute to the change of SRO in the 1NN shell. We utilize the example slip-planes shown in Fig. 4 to be consistent. As a function of the displacement, $\bar{\alpha}_{sum}^{1NN}$ varies in Fig. 6a. We can calculate the change of SRO parameters from initial state during the slip motion as follows,

$$\Delta\bar{\alpha}_{i-j}^{1NN,u_{\langle 112\rangle}} = \bar{\alpha}_{i-j}^{1NN}(u) - \bar{\alpha}_{i-j}^{1NN}(0) \tag{21}$$

where $u_{\langle 112\rangle}$ is the slip displacement (normalized by the Burgers vector). $\Delta\bar{\alpha}_{sum}^{1NN,u_{\langle 112\rangle}}$ can be similarly obtained by summing up each pair quantity. In Fig. 6b, we plot intrinsic SFE (γ_{isf}) and CRSS (screw dislocation) in the colormap by the change of SRO by the ISF point, $\Delta\bar{\alpha}_{sum}^{1NN,isf}$. The unstable and intrinsic SFEs (γ_{us}, γ_{isf}) of $Ni_{63.7}V_{36.3}$ alloy can respectively range by 165.4 mJ/m^2 ~ 356.1 mJ/m^2, and 1.71 mJ/m^2 ~ 265.5 mJ/m^2, while the CRSS varies 1.28 MPa ~ 226.3 MPa. The increase of SFEs results in the CRSS enhancement, which is also found for general FCC materials in the previous works (Celebi et al., 2023; You et al., 2023b).

The trend of "SRO change" by the ISF point, $\Delta\bar{\alpha}_{sum}^{1NN,isf}$, is well captured in colormap by following the propensity between CRSS and γ_{isf}. The largely negative $\Delta\bar{\alpha}_{sum}^{1NN,isf}$ corresponds to higher CRSS and γ_{isf}, while the positive $\Delta\bar{\alpha}_{sum}^{1NN,isf}$ can even yield less than 10 MPa. The positive $\Delta\bar{\alpha}_{sum}^{1NN,isf}$, however, is not physically preferred in short-range ordered materials, whereas chemically random configuration may have the positive $\Delta\bar{\alpha}_{sum}^{1NN,isf}$. The data statistics also summarize that 19 data out of 108 (17.6 %) show positive $\Delta\bar{\alpha}_{sum}^{1NN,isf}$ cases and these are only in random and intermediate configurations of the MD/MC simulation. Therefore, the negative $\Delta\bar{\alpha}_{sum}^{1NN,isf}$ is statistically preferred, and it would result in the higher CRSS and γ_{isf}. Also, since the highest stress barrier should be overcome in the macroscale deformation, we assign the "highest CRSS" as a solution among the multiple slip-planes and structures.

The current definition of SRO during slip motion is based on the local composition in the slip-plane and the change of the pair probability defined in the WS cell. The probability change originates from the bond broken/restored mechanism. This similar mechanism has been shown to correlate γ_{isf} and change of charge density (Kioussis et al., 2002; Qi and Mishra, 2007; Zhao et al., 2019), which requires another computational cost. The change of SRO $\Delta\bar{\alpha}_{sum}^{1NN,u_{\langle 112\rangle}}$ can efficiently guide the SFEs (γ_{us}, γ_{isf}) for multiple slip-planes with reduced DFT calculations. Also, $\Delta\bar{\alpha}_{sum}^{1NN,u_{\langle 112\rangle}}$ can further improve the estimation of the SFEs (γ_{us}, γ_{isf}) by applying the previous Cohen and Fine (1962) formula,

$$\gamma = \frac{\Delta\varepsilon - T\Delta s}{A} \tag{22}$$

where $\Delta\varepsilon$ is the change of total energy, Δs the change of entropy during slip, and A the slip-plane area. $\Delta\varepsilon$ can be also defined as

$$\Delta\varepsilon = 2c_i c_j \sum_m \sum_{pair} \sum_{i-j} Z_m U_{i-j} \Delta\alpha^m \tag{23}$$

where c_i and c_j are the concentrations of i and j atomic species, Z_m the coordination number for the m-th shell, U_{i-j} the interaction energy of $i-j$ pair, and $\Delta\alpha^m$ the change of SRO for the m-th shell. For 0 K, Eqn. (22) is reduced to direct relation between SFE and $\Delta\varepsilon$. Also, we focus on the SRO parameters defined in the WS cell, so only $\sum U_{i-j}\Delta\alpha^{1NN}$ term is considered. We then substitute $\Delta\bar{\alpha}_{i-j}^{1NN,u_{\langle 112\rangle}}$ into $\Delta\alpha^{1NN}$, resulting in $\sum U_{i-j}\Delta\bar{\alpha}_{i-j}^{1NN,u_{\langle 112\rangle}}$.

In Fig. 7, we demonstrate the further improved estimation of γ_{isf} by using the SRO change weighted by the interaction energy, $\sum U_{i-j}\Delta\bar{\alpha}_{i-j}^{1NN,isf}$. In Fig. 7a, the interatomic energy on each pair is obtained by DFT calculations. In a large cubic cell (20 Å × 20 Å × 20 Å), two atoms are isolated and incrementally spaced by interatomic distance, r. Then data is fitted by the standard Lennard-Jones (1931) form. We use the minimum interatomic energy at r_m, where $\frac{dE}{dr}]_{r_m} = 0$, for each pair as a constant interaction term U_{i-j}, given by

$$U_{i-j} = E(r_m) \tag{24}$$

The interaction term of each pair is obtained as $U_{Ni-Ni} = -4.21$ eV, $U_{Ni-V} = -7.20$ eV, and $U_{V-V} = -9.85$ eV. In Fig. 7b, γ_{isf} is estimated by the change of SRO based the WS-cell incorporated with the weighted summation by interaction energy $\sum U_{i-j}\Delta\bar{\alpha}_{i-j}^{1NN,isf}$. For the average SRO change $\Delta\bar{\alpha}_{i-j}^{1NN,isf}$, the corresponding average γ_{isf} is shown. The distributions of $\sum U_{i-j}\Delta\bar{\alpha}_{i-j}^{1NN,isf}$ and γ_{isf} are given in Fig. S3 in the Supplementary Materials. Most of data is on the positive and zero $\sum U_{i-j}\Delta\bar{\alpha}_{i-j}^{1NN,isf}$ (i.e., negative and zero $\Delta\bar{\alpha}_{i-j}^{1NN,isf}$). The quantity of $\Delta\bar{\alpha}_{i-j}^{1NN,isf} = 0$ corresponds to the same atomic species (in Layer$_{-1}$) restored in its WS cell during slip motion (unlike Fig. 5). This may be statistically close to the case of the slip in long-range (fully) ordered phases such as $L1_1$- or $L1_2$-type since the slip in the ordered materials also leads to zero quantity of $\Delta\bar{\alpha}_{i-j}^{1NN,isf}$ in plane-configuration (Layer$_{(-1,0)}$).

3.3. Effect of solute concentration

In this section, we investigate the effect of V solute concentration in material properties and compare the results with experiment. In Fig. 8, the effect of V composition on bulk (macroscopic) properties is demonstrated. The lattice constant is gradually increasing with V concentration in Fig. 8a, which agrees well with the experiment (Smith et al., 1982). This results from the introduction of the vanadium atoms to the nickel lattice and the associated lattice expansion. The variation of lattice constant with V concentration is 10 times larger than the one with the SRO in Fig. 3. This variation to the CRSS, however, will be negligible in different V concentrations since the larger variation (~ 0.3 Å) is needed to significantly change the CRSS (You et al., 2023b). In the meanwhile, the elastic constants are gradually decreasing in both (μ, C_{44}) in Fig. 8b, which are double contributions in the CRSS increase, although their

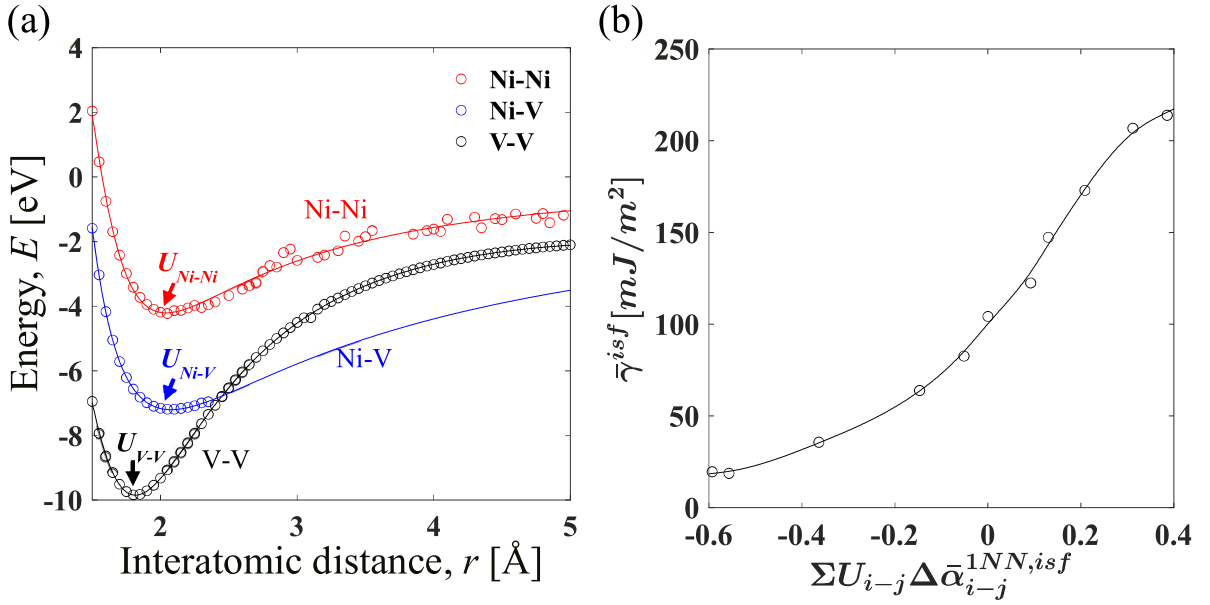

Fig. 7. Modeling intrinsic stacking fault energy (γ_{isf}) based on interaction energy and the change of SRO; (a) Determination of interaction energy of each pair considered in Ni-V alloy; b) $\Delta\bar{\alpha}_{i-j}^{1NN,isf}$ multiplied by a pair-wise interaction energy component and its direct estimation for average intrinsic stacking fault energy ($\bar{\gamma}_{isf}$).

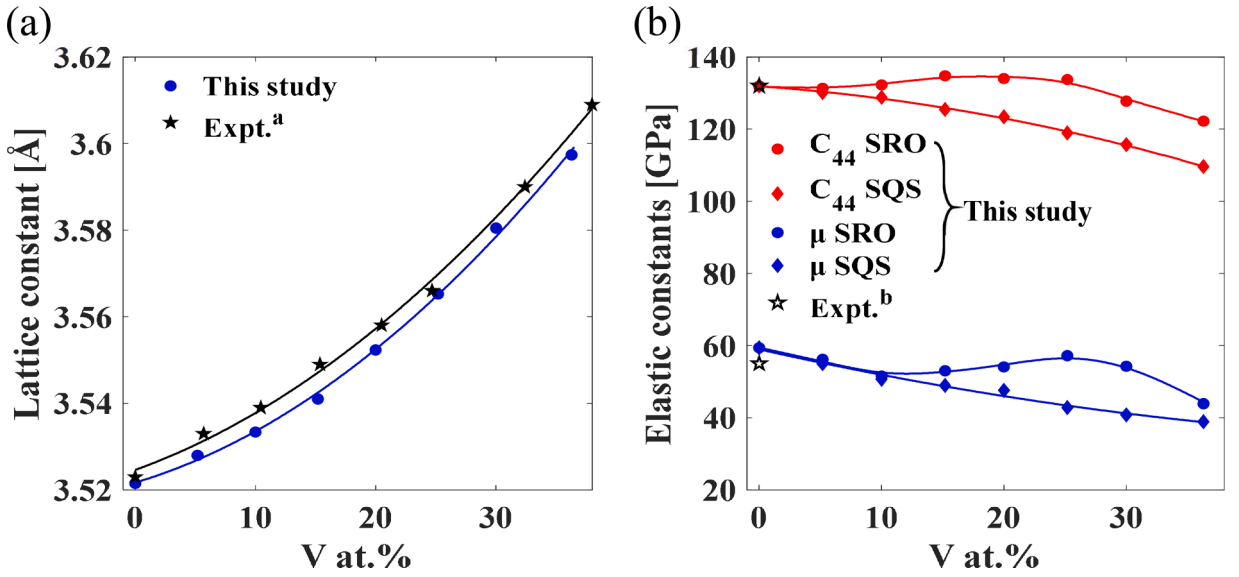

Fig. 8. Compositional effect on bulk properties in Ni-V; (a) Lattice constants of final MC/MD structures at each composition; Experimental lattice constants (Expt.[a]) are extracted from elsewhere (Smith et al., 1982), measured at room temperature, (b) Elastic constants (μ, C_{44}) of SRO and SQS structures at each composition; Experimental constants for pure Ni (Expt.[b]) are from Ref. (Simmons and Wang, 1971), measured at low temperature.

variations are up to ~ 20 GPa. The gap of elastic constants between random (SQS) and final MC/MD (SRO) structures is also varying with V concentration. The lower V concentration makes this gap smaller, since there is less possibility for V atom to occupy different configurations. This can be also applied to the variations of SFEs within V concentration.

We investigate the effect of V concentration on the CRSS in the alloys. The determination of CRSS based on the MCS framework requires input variables (lattice constant, C_{11}, C_{12}, C_{44}, γ_{us}, and γ_{isf}). The investigation of unstable and intrinsic SFEs (γ_{us}, γ_{isf}) in this study has been implemented in multiple slip-planes and configurations for all compositions as similar to Fig. 6b. Then the CRSS has also a range in other compositions as well, and we consistently show the "highest CRSS" among different slip-planes for all compositions in

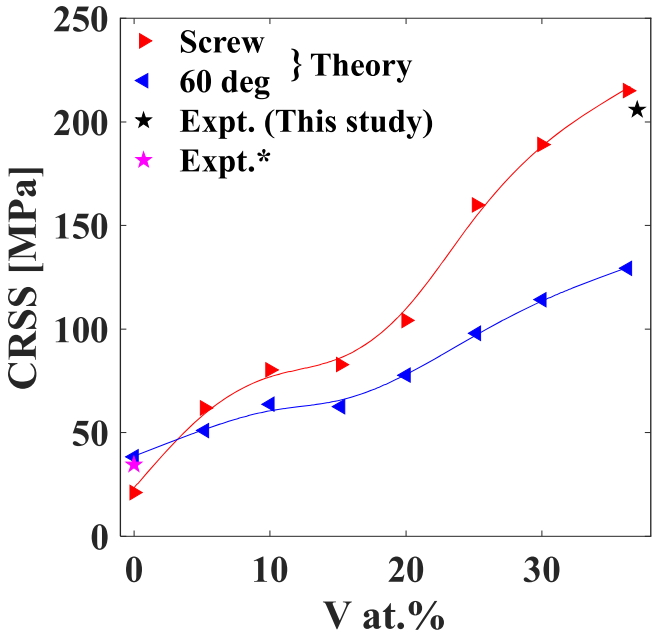

Fig. 9. Compositional effect on CRSS in Ni-V; The maximum CRSS among different slip-planes and structures for screw and 60° mixed dislocation characters; Experimental strength for pure Ni (Expt.*) is exploited from Ref. (Wu et al., 2014). For $Ni_{63.7}V_{36.3}$ alloy, additional experiments are conducted with polycrystalline samples in different temperatures and the Hall-Petch correction is incorporated (See Appendix (A). Experimental CRSS for Ni and $Ni_{63}V_{37}$ alloy are obtained by taking Taylor factor at zero temperature-extrapolation.

Fig. 9, as discussed in Fig. 6b. We calculate the CRSS for both screw and 60° mixed dislocations, since these are the possible dislocation characters that have the extreme CRSS (Celebi et al., 2023). The increase of CRSS in V 5 at.% ~ 10 at.% compared to pure Ni is mainly attributed to the elastic constants, since they have similar SFE values to pure Ni. However, the CRSS in screw dislocation becomes dominant in alloys because γ_{isf} gets close to γ_{us} barrier, which has been also found at pure aluminum (Celebi et al., 2023). In Table 1, we tabulate the input material constants that have shown the largest CRSS among all slip-planes and structures considered in each composition. The SFEs (γ_{us}, γ_{isf}) in V 36.3 at.%, for instance, (320.4 mJ/m^2, 236.6 mJ/m^2) is showing the highest CRSS among 108 data in Fig. 6b including all possible "SRO change", $\Delta\bar{\alpha}_{sum}^{1NN,isf}$ in different slip-plane configurations. Although the intermediate compositions (V 20 at.%, 25 at.%, 30 at.%) irregularly have higher SFEs (γ_{us} or γ_{isf}) than V 36.3 at.%, there are also elastic constants decreasing and change of γ_{us}-γ_{isf} ratio, which can enhance the strength in V 36.3 at.%. The contribution of each parameter to the CRSS has been shown in the previous studies (Celebi et al., 2023; You et al., 2023a, 2023b).

The CRSS in Fig. 9 and SFEs in Table 1 have been compared with other computations or experiments in good agreement. The SFEs (γ_{us}, γ_{isf}) of pure Ni (299.0 mJ/m^2, 137.6 mJ/m^2) are comparable to the previous work (292.0 mJ/m^2, 134.0 mJ/m^2) (Celebi et al., 2022). The experimental CRSS for pure Ni is exploited from elsewhere (Wu et al., 2014), and for $Ni_{63.7}V_{36.3}$ alloy, it has been reported to have yield stress ~ 750 MPa with grain size ~ 8.1 μm at room temperature (Oh et al., 2019). This is, however, insufficient to compare with the theory in this work since it has only one data in grain size and temperature dependencies. Therefore, we conduct additional experiments in this study. Details are elaborated in Appendix A. We obtain yield stresses of $Ni_{63}V_{37}$ alloy ~ 570 MPa and ~ 410 MPa at 77 K and 298 K, respectively, and the average grain size as ~ 0.15 mm. The Hall-Petch coefficient is determined as k_y ~ 1248 MPa·μm^{½}, based on available data including reference and current study. We then estimate the CRSS for single crystal $Ni_{63}V_{37}$ alloy at two temperatures as ~ 152 MPa and ~ 102 MPa by using Taylor factor ($M = 3.06$). These agree well with theoretical predictions of CRSS using SFEs at finite temperatures (See Appendix A). The experimental CRSS estimated at zero-temperature is evaluated by ~ 206 MPa, which is also in the range of theoretical prediction 215.1 MPa (screw dislocation). We acknowledge that the current study has been compared with a limited number of experimental data available in SFEs and CRSS, which requires further studies such as for various vanadium concentrations and higher temperatures.

In Fig. 10, we further illustrate the equilibrium dislocation core structures by the MCS framework. The V compositional effects on the core-width and partial separation distance (i.e., SFW) are depicted in Fig. 10a and b. The core-width propensity with V concentration is oppositely similar to the CRSS. The leading partial (LP) core-width ξ_{LP} is decreasing by V concentration, i.e., narrower core which results in higher CRSS, and ξ_{LP} for 60° mixed character is larger than the one for screw dislocation, since the core-widths of mixed dislocation characters usually have asymmetricity between ξ_{LP} and ξ_{TP}, trailing partials (TP). The SFWs for two dislocation characters, on the contrary, represent different propensity with V concentration. The SFW for screw dislocation is smaller than 60° mixed character, which also found in other FCC materials. The highest CRSS at 36.3 at.% of V corresponds to the lowest SFW in 60° mixed dislocation. In the V concentration range from 15 at.%, the SFW becomes smaller than the core-width ($< 2.5\, b_p$), meaning that the core structures of LP and TP are overlapped each other. Then Ni-V alloys exceeding 20 at.% of V concentration illustrate infinitesimally small SFW, almost full dislocation structure. This is schematically shown in Fig. 10c. This undissociated structure is attributed to the small difference between the unstable and intrinsic SFEs (γ_{us}, γ_{isf}), being similar to pure aluminum (Celebi et al., 2023), and this fact results in the higher CRSS for screw dislocation rather than 60° mixed dislocation character.

Regarding the core-width and the CRSS dependence, our previous work showed an increase in CRSS by decreasing the lattice constant (You et al., 2023b) in the range 6 to 3 Angstroms- the relationship is nonlinear. The effect of increasing V in Ni-V alloy is to increase the lattice constant from 3.5 Å to 3.6 Å, which is a relatively a small range and hence has a secondary effect on CRSS. On the other hand, surmounting a higher energy barrier corresponding to a higher local "SRO change" (Fig. 6b) has a significant effect on the CRSS. We note that lattice constant and elastic moduli are bulk properties before the slip occurs, so they are influenced by the initial SRO, but the "SRO change" is the key parameter to dictating the CRSS.

4. Final comments

In this work, we mainly found the contribution of the "SRO change" upon slip, not the initial SRO state, to the strengthening. Most recent studies in this field have often considered only "as-cast SROs" based on the existence of extra reflections in electron diffraction

Table 1
Compositional effect on fault energies in Ni-V; Stacking fault energies that resulted in the maximum CRSS at each composition; At each V composition from 5 at.% to 30 at.%, a total of 16 data is investigated within 2 structures; For 36.3 at.% of V, 108 data within 12 structures are included; SFEs (γ_{us}, γ_{isf}) of pure Ni is comparable with (292.0 mJ/m^2, 134.0 mJ/m^2) from Ref. (Celebi et al., 2022).

Material	a [Å]	C_{11} [GPa]	C_{12} [GPa]	C_{44} [GPa]	γ_{us} [mJ/m^2]	γ_{isf} [mJ/m^2]	CRSS (Screw) [MPa]	CRSS (60°) [MPa]
Ni	3.522	276.8	158.0	132.0	299.0	137.6	21.1	38.3
$Ni_{94.8}V_{5.2}$	3.528	277.6	165.2	131.3	304.3	148.7	61.9	51.0
$Ni_{90}V_{10}$	3.533	277.1	173.9	132.3	312.5	183.8	80.3	63.7
$Ni_{84.8}V_{15.2}$	3.541	281.2	175.1	134.8	305.1	208.1	82.8	62.6
$Ni_{80}V_{20}$	3.552	284.3	176.1	134.0	337.2	206.3	104.2	77.8
$Ni_{74.8}V_{25.2}$	3.565	287.8	173.4	133.7	358.9	303.5	159.9	98.0
$Ni_{70}V_{30}$	3.580	281.9	173.4	127.8	371.1	281.3	189.1	114.2
$Ni_{63.7}V_{36.3}$	3.604	258.7	176.5	115.0	320.4	236.6	215.1	129.3

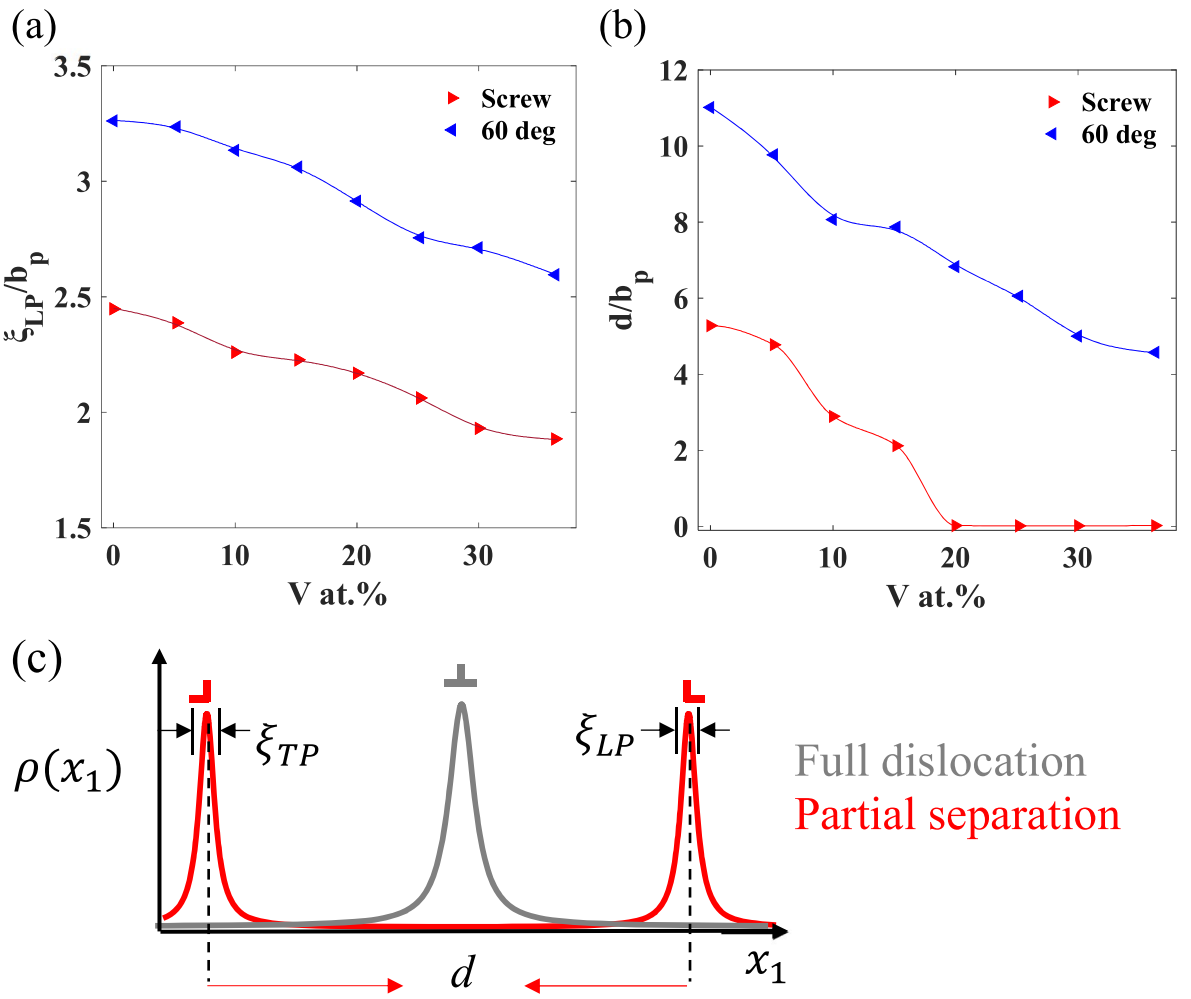

Fig. 10. Equilibrium dislocation core structures of Ni-V binary alloys by different compositions where the slip-plane is dictated by the maximum CRSS; (a) Core-widths; and (b) stacking fault width (SFW; *d*) for screw and 60° mixed dislocation characters; Both are normalized in partial Burgers vector, b_p; (c) the schematic of undissociated and dissociated dislocation (full dislocation and partial separation).

patterns. However, the role of SRO to the strengthening has been frequently questioned since theoretical explanation based on crystallography used to conflict with the experimental findings such as missing or abundant reflections. We reevaluate the previous concept of SRO variation suggested by Cohen and Fine (1962), but carefully formulate the SRO characterization to accurately connect it to the strengthening. In Appendix B, we demonstrate the SRO variation upon slip in close-packed view and compare our approach with the one of Cohen-Fine. The concept by Cohen-Fine only utilizes the initial SRO values for the prefixed coordination shells. It does not consider the actual change of constituent atoms lying in the neighbor shells from the center atom, which results in inaccurate prediction to the strengthening. In this work, the SRO characterization upon slip considers the correspondingly updated coordination shells at each disregistry. Based on the WS cell, the broken or restored atomic pair is carefully considered in the short-range domain. Therefore, the results of CRSS and SFEs show an insightful correlation with the "SRO change" upon slip.

The current results of CRSS and SFEs in FCC Ni-V alloys agree well with the experimental results, although they are limited. One may still question the role of "SRO change" to the strengthening in experiment since the contribution of SRO (initial SRO) has been also controversial as commented above. A recent study (Walsh et al., 2023), nevertheless, has pointed out that the extra electron reflections in diffraction patterns may be ascribed to planar defects, not the as-cast SRO. Another experimental study also found that the evolution of SRO during the mechanical strain is characterized by in-situ electron diffraction (Seol et al., 2022). Both studies pointed out the role of SFs to the strengthening, which strongly supports our approach. Our SRO strengthening framework is to incorporate the planar "SRO change" in the WS cell during slip motion, and it is correlated well with the SFEs by simply combining the weight of interaction energies. To further emphasize our approach in the consistency with the experiments, we demonstrate the virtual diffraction analysis of slipping planes in Appendix C. We model the FCC unit-cell motifs in the WS cell to reproduce the planar diffraction images. The changes of intensity of diffraction pattern in different slip-planes show good agreement with the SRO changes for $Ni_{63.7}V_{36.3}$ alloy.

Finally, we also emphasize that the "SRO change" in the WS cell upon slip can accurately predict the SFEs. This can reduce hundreds

of DFT calculations for the SFEs. The acquisition of accurate interaction energy might be less accessible than the calculation of SRO variation, although simply applying the standard diatom method still gives us a great prediction. For efficient utilization of current theory, the negatively maximum SRO change on the slip-plane guides us to know the prevailing CRSS in the given atomic configuration. For different solute compositions, this still holds although the negative limit of SRO change may vary, which has similar correlation with the maximum CRSS variation in V solute compositions (See Appendix D). The current theory applied to Ni-V alloys is validated by using additional experiments and AIMD in finite temperatures, both which are not covered previously. One can still apply the current approach to the classical MD as well by using its own empirical potential and a large superlattice. The extensions of this work to other material systems (e.g., medium- and high-entropy alloys), and crystal structures (e.g., hcp, bcc) remain future studies as well.

CRediT authorship contribution statement

Daegun You: Formal analysis, Investigation, Methodology, Software, Validation, Visualization, Writing – original draft, Writing – review & editing. **Orcun Koray Celebi:** Conceptualization, Investigation, Methodology, Software, Writing – original draft, Writing – review & editing, Supervision. **Gorkem Gengor:** Conceptualization, Investigation, Methodology, Software, Supervision, Writing – original draft, Writing – review & editing. **Ahmed Sameer Khan Mohammed:** Conceptualization, Investigation, Methodology, Software, Supervision, Writing – original draft, Writing – review & editing. **Wael Abuzaid:** Investigation, Methodology, Resources, Validation, Writing – review & editing. **Huseyin Sehitoglu:** Conceptualization, Funding acquisition, Investigation, Project administration, Supervision, Writing – review & editing.

Declaration of competing interest

The authors declare that they have no known competing financial interests or personal relationships that could have appeared to influence the work reported in this paper.

Data availability

Data will be made available on request.

Acknowledgment

The work is supported by the National Science Foundation (NSF) under award number CMMI-21–25821, which is gratefully acknowledged. In addition, the use of the Illinois Campus Cluster, a computing resource that is operated by the Illinois Campus Cluster Program (ICCP) in conjunction with the National Center for Supercomputing Applications (NCSA) and which is supported by funds from the University of Illinois at Urbana-Champaign, is also gratefully acknowledged.

Supplementary materials

Supplementary material associated with this article can be found, in the online version, at doi:10.1016/j.ijplas.2024.103919.

Appendix A: Theoretical and experimental validation in finite temperatures

The field of atomistic simulations has been the focus of studies at 0 K without thermal effects while many of the experiments are conducted between 77 K and room temperature. Only in rare cases, there are experiments available at 4 K. The lattice resistance calculated at 0 K provides an important baseline for considerations of CRSS at finite temperatures. In this section, we review the experiments at liquid nitrogen (LT) temperature, 77 K, and at room temperature (RT), 298 K, on $Ni_{63}V_{37}$ and show our predictions at different temperatures.

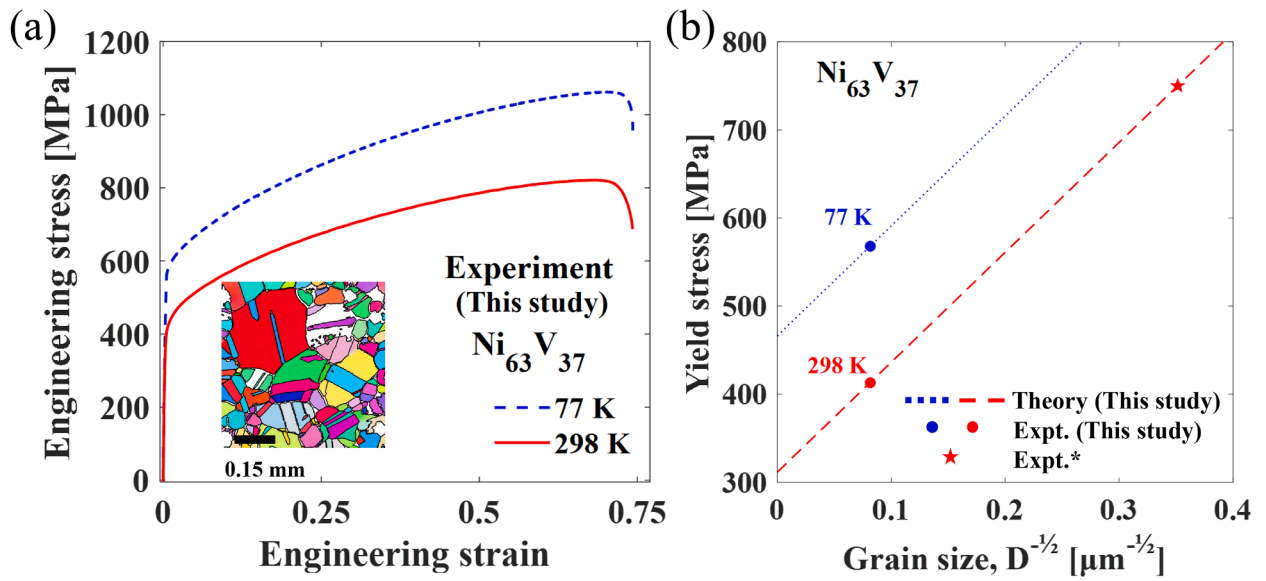

Fig. A1. Tensile experiments of $Ni_{63}V_{37}$ binary alloy in different temperatures. (a) Tensile stress-strain curves at liquid nitrogen (LT, 77 K) and room temperature (RT, 298 K); Microstructure image is shown in the inset to get average grain size (~ 0.15 mm). (b) Incorporation of Hall-Petch contribution in $Ni_{63}V_{37}$ alloy to obtain the CRSS; Theory in this study with experiment from this study and from elsewhere (Expt.*) (Oh et al., 2019) is included with data symbols.

The binary $Ni_{63}V_{37}$ alloy (in atomic fraction) was arc-melted using pure elements (purity > 99.9 at.%). Following casting, the ingot was homogenized at 1200 °C for 24 h in an Ar atmosphere. The nominal composition and homogeneity of the ingot was confirmed by using energy dispersive spectroscopy. 4 mm thick strips were machined from the cast material and cold rolled to about 75% thickness reduction. Tensile specimens were subsequently machined from the homogenized ingot using electrical discharge machining. The dog-bone samples had 3 × 1.26 mm cross-section and 8 mm gauge-length. Prior to loading in each temperature, the solution heat-treatment was applied to all specimens at 1100 °C for 1 h, in air, followed by quenching in water to assure a single phase, FCC structure, which was confirmed using X-ray diffraction (Fig. S4 in the Supplementary Materials). Tensile experiments were conducted at two different temperatures such as LT (77 K) and RT (298 K). An Instron load frame was used to apply the tensile loading. For an experiment conducted at LT, the entire sample and loading grips were submerged in a liquid nitrogen bath prior to loading. The deformation was applied using displacement control with an average strain rate of ~ 10^{-3} s^{-1}.

In Fig. A1a, tensile stress-strain curves of $Ni_{63}V_{37}$ alloy at LT and RT are shown. The yield stresses for two temperatures are determined as ~ 570 MPa and ~ 410 MPa, respectively. Two or three times of tensile tests are repeated with high reproducibility (Fig. S5 in the Supplementary Materials). We also obtained the microstructure image using scanning electron microscopy (SEM). One of the SEM images is shown in the inset figure, and the average grain size of polycrystalline $Ni_{63}V_{37}$ alloy is determined as ~ 0.15 mm. Given the yield stresses and average grain size, we further calculated the Hall-Petch contribution to estimate the CRSS in single crystal in Fig. A1b. The Hall-Petch equation is defined as follows, $\sigma_y = \sigma_0 + k_y/\sqrt{D}$ where σ_y the yield stress, σ_0 the lattice friction, k_y the Hall-Petch coefficient, and D is the grain size, respectively. We referred the yield stress data (~ 750 MPa) of $Ni_{63.2}V_{36.8}$ for smaller grain size (~ 8.1 μm) at RT from elsewhere (Oh et al., 2019). For the RT, the Hall-Petch coefficient is determined as k_y ~ 1248 MPa·μm^{½}. Based on available data, we assumed the same Hall-Petch coefficient at the LT, and then obtained the lattice friction stresses at LT and RT as σ_0 ~ 466 MPa and ~ 312 MPa, respectively. Although some materials showed an increase of the Hall-Petch coefficient with decreasing temperature (Liu et al., 2023; Sun et al., 2019), it would have approximately a 5 % effect on the results but would not change the conclusion of this study. Therefore, we estimated the CRSS for single crystal $Ni_{63}V_{37}$ alloy at two temperatures as ~ 152 MPa and ~ 102 MPa by using Taylor factor ($M = 3.06$) substituted in CRSS $= \sigma_0/M$. In the following paragraph, we compared these experimental results to the theory given in this work by accommodating ab-initio MD simulations for SFEs in finite temperatures.

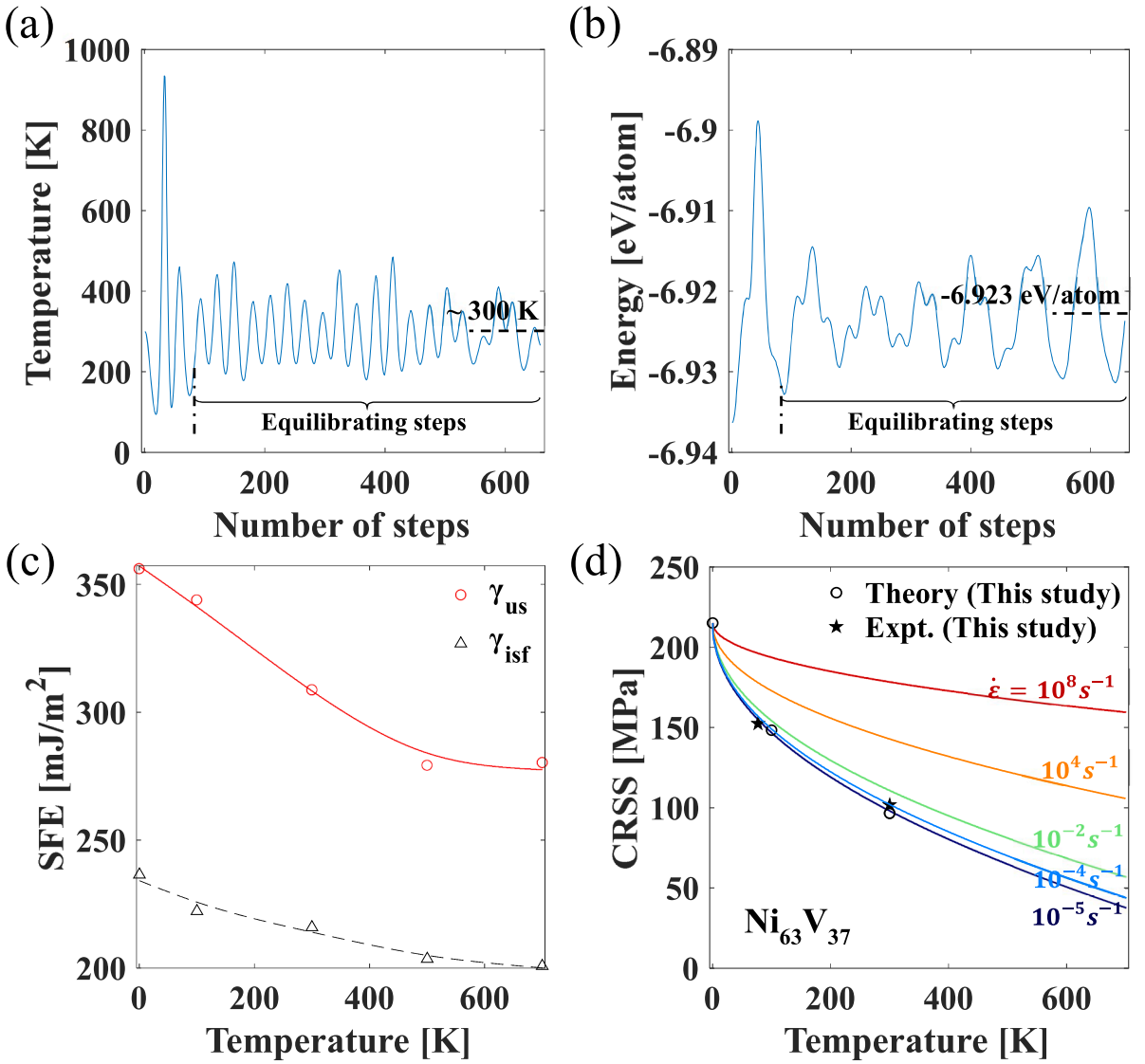

Fig. A2. Theoretical CRSS prediction of $Ni_{63.7}V_{36.3}$ alloy in finite temperatures using Ab-initio molecular dynamics (AIMD) simulation. (a) Temperature fluctuation of $Ni_{63.7}V_{36.3}$ alloy in AIMD; Example is shown for 300 K target; Temperature is stabilized to ~ 300 K in average. (b) Energy fluctuation for 300 K target. (c) Stacking fault energies (SFEs) of $Ni_{63.7}V_{36.3}$ alloy at the specific slip-plane that the maximum CRSS occurs at 0 K from the final configuration in hybrid MC/MD. (d) Comparison of theoretical and experimental CRSS of $Ni_{63}V_{37}$ alloy in this study.

For finite temperature prediction of SFEs in this work, we use ab-initio molecular dynamics (AIMD). This approach does not rely on 1) the empirical interatomic potential that is commonly used in the classical MD, and 2) the extrapolation of free energy from 0 K (such as quasi-harmonic approximation), so that we can more accurately estimate the SFEs in finite temperatures. For the electronic-structure problem in AIMD, we use the same PAW-PBE pseudopotentials for Ni and V. In this work, a Nosé-Hoover thermostat is chosen for drawing an equilibrium state from a canonical ensemble of sampled states (Hoover, 1985; Nosé, 1984). This introduces extra fields such as fictitious friction terms into the Hamiltonian such that,

$$H' = \sum_{i=1}^{N} \frac{m_i}{2} s^2 \dot{\vec{r}}_i^2 - U_p(\vec{r}) + \frac{Q}{2}\dot{s}^2 + 3NkT\ln(s) \tag{A1}$$

where N is total number of atoms, m the mass of atom in i site, s the fictitious parameter introduced, $\vec{r}$ the position of atoms, so that the first two terms are kinetic and potential energy (U_p) of the given system. Q is the effective mass of s, k Boltzmann constant, and T is the temperature. We set $Q = 1$, and the simulation is controlled in 2 fs time-step (total 600 ~ 700 steps, i.e., 1.2 ~ 1.4 ps), 450 eV plane-wave energy cut-off, and single k-point Γ mesh-grid. We initially applied the same superlattice optimized at 0 K for all the calculations. We only selected the one slip-plane that gives the maximum CRSS in the final configuration of hybrid MC/MD.

In Fig. A2, we summarize the theoretical results in finite temperatures. The equilibrated temperature along the time frame

approaches the target temperature on average for all the calculations. The proper equilibrating step is determined by the minimum error of mean, ϵ. The error of mean at each cutoff step (i) is defined by $\epsilon_i = \sqrt{\frac{V_i}{N_{t,i}/\kappa}}$, where V_i is variance, $N_{t,i}$ the number of data at each cutoff, and κ is correlation time based on autocorrelation such that $\kappa = 1 + 2\sum_{j=1}^{N_t} \frac{1}{V} \frac{1}{N_t - j} \sum_{k=1}^{N_t - j} (X_k - \overline{X})(X_{k+j} - \overline{X})$, and V, $\overline{X}$, and N_t are variance, average, and total number of data for original X without cutoff. We present an example of undeformed structure (before slip) at 300 K target in Fig. A2a and b. In this example, the cutoff for equilibrating step is determined by $i = 83$ with the minimum error of mean $\epsilon = 0.92$ K and autocorrelation time $\kappa = 9.62$. Total energy of undeformed structure also shows the converged value on average (denoted) by excluding the data in non-equilibrating steps. Similarly, the AIMD simulations on deformed structures at different temperatures directly enable the calculation of SFEs using equilibrated average values substituted in Eq. (3), since the resultant energies include thermal excitations and change of entropy. In Fig. A2c, both unstable and intrinsic SFEs (γ_{us}, γ_{isf}) exponentially drops as temperature increases. Using the SFE values and theory in this work, we obtain the CRSS in different temperatures in Fig. A2d, such as 162 MPa at LT and 97 MPa at RT, which agree well with the experimental results 152 MPa, and 102 MPa, respectively. We extrapolate experimental data to zero temperature CRSS ($\sim$ 206 MPa) in the main text for consistency. For the temperature extrapolation with experimental strengths, we use the following fitting formula (Wu et al., 2014), $\tau_y(T) = \tau_a \exp\left(-\frac{T}{C}\right) + \tau_b$, where τ_y is the CRSS, $\tau_a = 152.5$ MPa, $\tau_b = 53.4$ MPa, and $C = 245.1$ K. The fitting constants (τ_a, τ_b, C) are determined by using currently available data.

We also predict the CRSS with consideration of strain rate effect as well accompanied by temperature in Fig. A2d. We note that strain rate effect in the current framework has no significant within the range of 10^{-5} s^{-1} $\sim$ 10^{-2} s^{-1} by the following analysis. The common Arrhenius form of strain rate (Argon, 2007), $\dot{\varepsilon} = \dot{\varepsilon}_0 \exp\left(-\frac{\Delta G(\tau/\tau_0)}{kT}\right)$, where $\Delta G(\tau/\tau_0)$ is a stress-dependent activation energy of dislocation, $\Delta G(\tau/\tau_0) = \Delta G_0 \left(1 - \frac{\tau}{\tau_0}\right)^{\alpha}$, ΔG_0 represents thermal activation energy required to overcome lattice resistance without aid from external stress, τ_0 is CRSS at absolute zero temperature, respectively. The reference strain rate, $\dot{\varepsilon}_0 = b\overline{y}\rho_m \nu_0$, is determined ($\dot{\varepsilon}_0 = 2.18 \times 10^9$ s^{-1}) by substituting a typical value $\nu_0 = 5 \times 10^{11}$ s^{-1} by Argon, and $b = b_p$, $\overline{y} = b_p/2$, $\rho_m = \frac{1}{13A \times 18A}$ for the current study. Two experiments at both LT and RT with the same strain rate ($\dot{\varepsilon} = 10^{-3}$ s^{-1}) determine the fitting constants ΔG_0 and α as 2.962 eV and 2.0458, respectively. The ΔG_0 is in good agreement with the activation energy of V (2.939 eV) or Ni (2.956 eV) in Ni host system from the recent work (Wu et al., 2016). The CRSS predictions for different strain rates, say 10^{-5} s^{-1} $\sim$ 10^{-2} s^{-1}, at LT and RT are 148.3 $\sim$ 154.6 MPa and 93.9 $\sim$ 106.0 MPa, respectively. These predicted levels are in close agreement with those stresses from experiments. We illustrate more curves of representative strain rates such as 10^4 s^{-1} and 10^8 s^{-1} for visual comparison.

Appendix B: "SRO change" upon slip in the previous study and this work

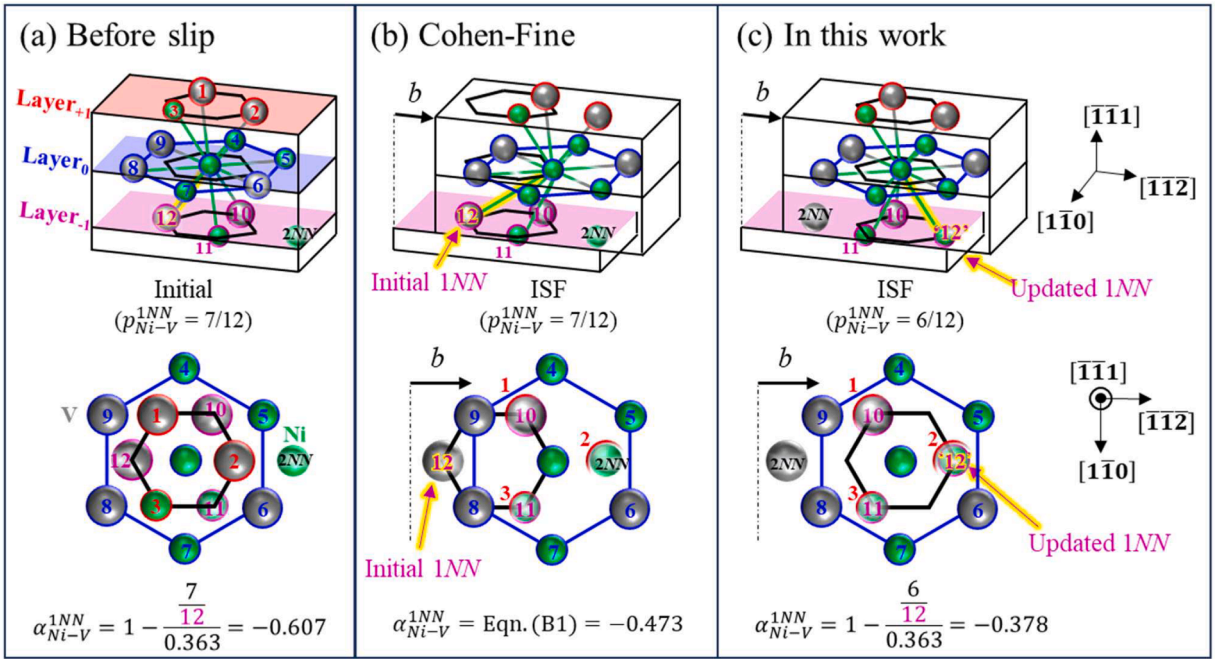

Fig. B1. Schematic of "SRO change" during slip motion in a single atom; (a) Both the previous (Cohen-Fine) and current studies characterize the SRO parameter the same at initial state. (b) Cohen-Fine suggested that SRO in prefixed shell numbers from initial state remains constants during entire slip disregistry. (c) In this work, SRO parameters are correspondingly updated as a slip-plane moves; Figure represents one slip motion in $[\overline{1}12]$ from initial to ISF state. Layer$_0$ is a slip-plane.

In this section, we describe the "SRO change" during slip motion with respect to the overall coordination in comparison with the

previous discussion. Cohen and Fine suggested that the SRO variation upon slip can contribute to the strengthening (Cohen and Fine, 1962). However, the coordination of SRO used in their model is fixed in entire slip motion. We represent it in the schematic in Fig. B1a-b. Before a slip occurs, the coordination in any NN shells is determined by every center atom in Layer_0, a slip-plane. For one center atom in Layer_0, as an example, Cohen-Fine characterized the SRO for the 1NN shell during slip motion as follows,

$$\alpha_{slip}^{1NN} = \frac{9\alpha_0^{1NN} + \alpha_0^a + \alpha_0^b + \alpha_0^c}{12} \tag{B1}$$

where α_0^{1NN} is the initial SRO value (before a slip occurs) for the 1NN shell, and the parameters (α_0^a, α_0^b, and α_0^c) are the initial SRO values for which a-th, b-th, and c-th NN shells of three atoms (such as 10, 11, 12 sites) are expected to lie in the 1NN range after a slip. For instance, before a slip occurs, the parameters (α_0^a, α_0^b, and α_0^c) are equal to α_0^{1NN}, so $\alpha_{slip}^{1NN} = \alpha_0^{1NN}$. After a slip motion in $[\overline{112}]$ direction, the parameters (α_0^a, α_0^b, and α_0^c) are expected to be α_0^{1NN}, α_0^{1NN}, and α_0^{2NN} at a typical ISF position, and α_{slip}^{1NN} becomes $\frac{11\alpha_0^{1NN}+\alpha_0^{2NN}}{12}$. The numeric such as 12 or 9 in Eq. (B1) is derived from total or partial coordination number for the 1NN shell such as within $\text{Layer}_{(-1,0,+1)}$ or $\text{Layer}_{(0,+1)}$. The unchanged coordination number for the 1NN shell that is only captured above Layer_{-1} becomes 9 (in $\text{Layer}_{(0,+1)}$) by subtracting 3 (in Layer_{-1}) from 12. If only the coordination in Layer_{-1} is considered (only three atoms), the SRO during slip motion was suggested as follows (Cohen-Fine),

$$\alpha_{slip}^{1NN,L_{-1}} = \frac{\alpha_0^a + \alpha_0^b + \alpha_0^c}{3} \tag{B2}$$

Similarly, at each initial or ISF point, $\alpha_{slip}^{1NN,L_{-1}}$ equals to α_0^{1NN} or $\frac{2\alpha_0^{1NN}+\alpha_0^{2NN}}{3}$, respectively.

The method suggested by Cohen-Fine utilizes the initial SRO values for the prefixed coordination shells. This method does not consider the true change of constituent atoms lying in the NN shells from the center atom. Also, it is not defined at the unstable barrier (USF point) during slip motion, since it does not consider the movement of NN shell by a slip. In this work, the SRO variation in the WS cell considers these aspects. In Fig. B1c for direct comparison (also in Fig. 5), the schematic of the SRO variation is represented for this study. During slip motion, all the coordination shells from the center atom are correspondingly updated at each disregistry. At ISF point, the atom previously bonded in the 1NN shell is defined in the 2NN shell, while another atom previously bonded in the 2NN shell is then defined in the 1NN shell. It is also described in the main text and Fig. 5 from initial to USF, and ISF points. By considering the actual change of the SRO upon slip motion, the SFEs and CRSS can be accurately predicted. We also compare the SRO variations during slip motion based on Cohen-Fine and current study in Fig. B2 and three major states are tabulated in Table B1. The average SRO of Ni-V pair ($\Delta\overline{\alpha}_{Ni-V}^{1NN,u_{\langle 112\rangle}}$) is shown in specific slip-plane (Plane B that is used for an example in Figs. 4 and 6) based on Eqs. (19)–(21). Based on initial SRO value, the one after a slip suggested by Cohen-Fine can be calculated by using either Eqs. (B1) or (B2). The estimation of SRO variation based on the previous study has discrepancy from the actual consideration of bond broken/restored mechanism in the shell movement.

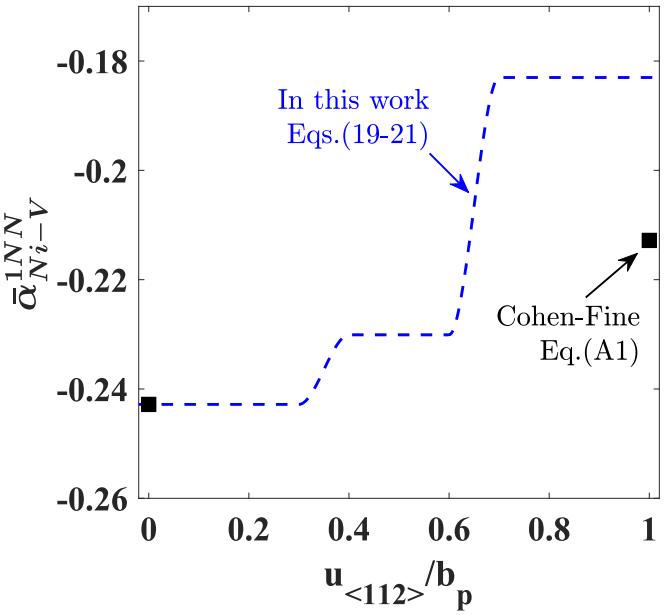

Fig. B2. Change of SRO based on the WS-cell (blue dashed line) and Cohen-Fine (black square) during slip motion; $\Delta\overline{\alpha}_{Ni-V}^{1NN,u_{\langle 112\rangle}}$ defined at slip-plane (Layer_0) varies upon slip deformation in current study, while the previous study is limited in the prefixed shell and discontinuity; A slip-plane stems from Plane B in Fig. 4 and 6 as a representation example.

Table B1

" SRO change" based on the WS-cell and Cohen-Fine during slip motion; $\Delta\overline{\alpha}_{Ni-V}^{1NN,u_{(112)}}$ at three major states (initial, USF, ISF) are shown; The magnitudes of SRO changes between two show a large discrepancy.

$\overline{\alpha}_{Ni-V}^{1NN,slip}$	$\overline{\alpha}_{Ni-V}^{1NN,0}$	$\overline{\alpha}_{Ni-V}^{1NN,us}$	$\overline{\alpha}_{Ni-V}^{1NN,isf}$	$\frac{\Delta\overline{\alpha}_{Ni-V}^{1NN,isf}}{\overline{\alpha}_{Ni-V}^{1NN,0}}$ (%)
This work	−0.243	−0.230	−0.183	24.6
Cohen-Fine	−0.243	–	−0.213	12.4

Appendix C: Virtual diffraction patterns of slip plane

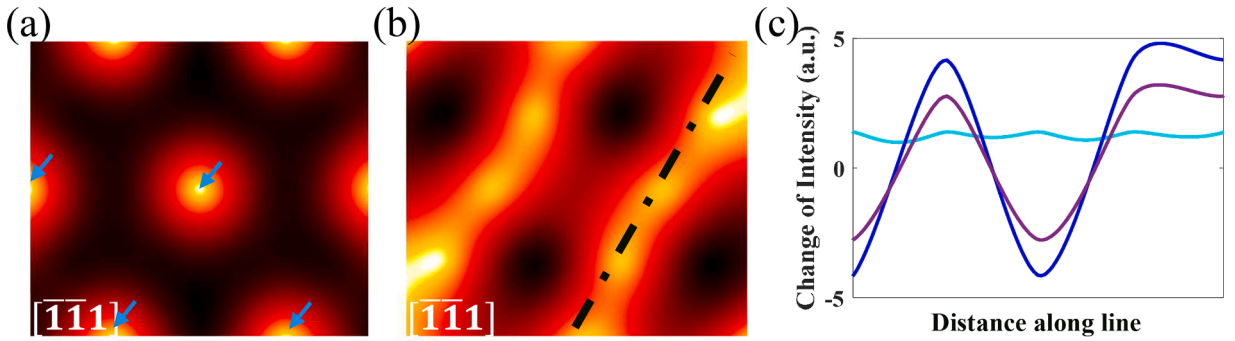

Fig. C1. Virtual diffraction patterns and intensities of $Ni_{63.7}V_{36.3}$ alloy upon slip; (a) Diffraction pattern of a slipping plane (Plane–A defined in Fig. 4 in the main text) in $[\bar{1}\bar{1}1]$ zone axis; Blue arrows denote the streaking of {110} planes, (b) Change of intensity of diffraction pattern of Plane–A in $[\bar{1}\bar{1}1]$ zone axis upon slip to isf point; dashed line for figure c, and (c) line profile of change of diffraction intensity for different slip-planes (Plane–A, B, and C defined in Fig. 4).

Recent studies for the SRO often claim its contribution to strength based on the existence of extra reflection spots. The main point in this work is the change of SRO in the WS cell upon slip motion, and its contribution to the strengthening. Therefore, we demonstrate virtual diffraction analysis based on unit-cell motifs by the following procedures. We take two layers ($Layer_0$ and $Layer_{-1}$) for one slip-plane and build the WS cell that can cover 3 atoms in $Layer_{-1}$ from the 1 center atom in $Layer_0$. Then each WS cell includes 1 unit-cell motif (4 atoms) for different diffraction pattern intensity. Since one layer has 30 atoms, we average the different diffraction pattern intensities from 30 WS cells for one slip-plane. In Fig. C1a, we depict a diffraction pattern of $Ni_{63.7}V_{36.3}$ alloy in a slipping plane (Plane–A defined in Fig. 4 in the main text) in $[\bar{1}\bar{1}1]$ zone axis. We also characterize the streaking of {110} planes (blue arrows) in the virtual diffraction pattern. In Fig. C1b, the change of intensity of diffraction pattern of Plane–A in $[\bar{1}\bar{1}1]$ zone axis is represented. Two diffraction patterns from initial and isf points are subtracted. For the line profile analysis, we define the example line (dashed line) in the diffraction and plot the change of diffraction intensities for different slip-planes (Plane – A, B, and C defined in Fig. 4) are demonstrated in Fig. C1c. The changes of SRO in pair summation $\Delta\overline{\alpha}_{sum}^{1st,isf}$ in three different slip-planes (Plane – A, B, and C) are –0.023, –0.096, and –0.091, respectively. The change of intensity in each slip-plane is also following this trend such that the smallest change of intensity in Plane – A, the largest change in Plane – B, and the one in Plane – C is an intermediate among three. Our claim for the SRO strengthening is based on the plane SRO variation upon slip, not the bulk SRO of initial state, which is consistent with the virtual diffraction pattern analysis here.

Appendix D: "SRO change" effect in γ_{isf} within solute concentrations

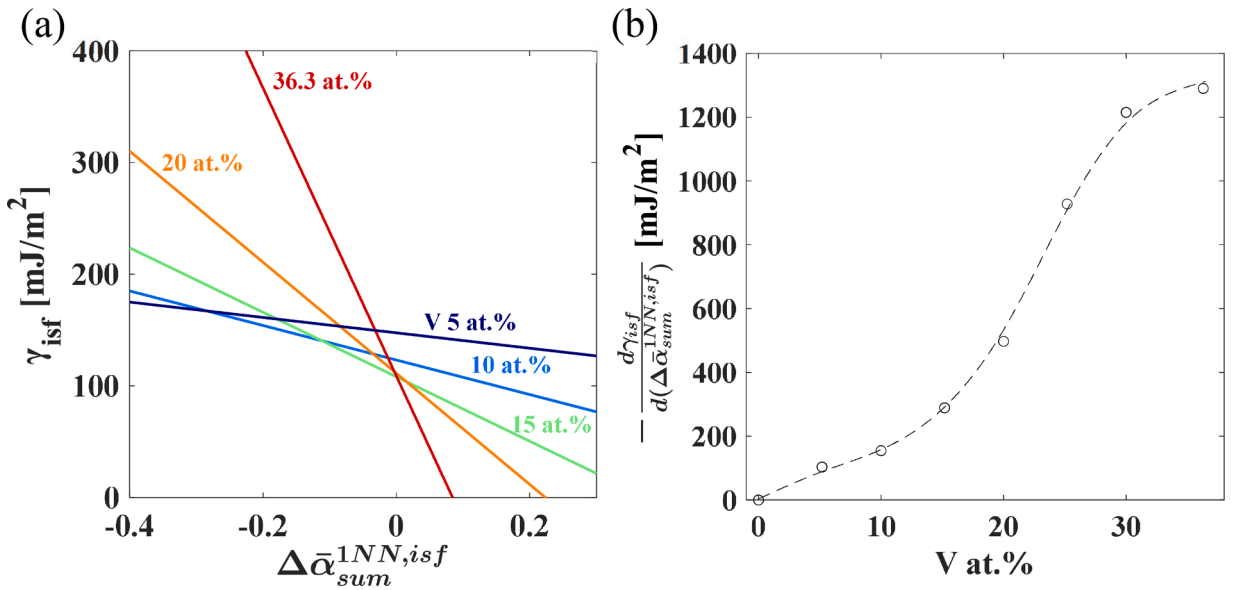

Fig. D1. Correlation between γ_{isf} and the SRO change in different V solute compositions. (a) Linear relation between γ_{isf} and the SRO variation ($\Delta\bar{\alpha}_{sum}^{1NN,isf}$) in each V composition; For simple visualization, the linear fitting in 25 at.% and 30 at.% compositions are not depicted. (b) Slope between γ_{isf} and $\Delta\bar{\alpha}_{sum}^{1NN,isf}$ in each V composition.

In this section, we further analyze the correlation between SFE and "SRO change" in different V solute compositions. As the correlation between the SRO variation, CRSS, and γ_{isf} for $Ni_{63.7}V_{36.3}$ alloy is shown in Fig. 6 in the main text, the linear correlations between the SRO variation and γ_{isf} for other compositions are also expected. In Fig. D1a, we plot the linear fitting of γ_{isf} versus the SRO change ($\Delta\bar{\alpha}_{sum}^{1NN,isf}$) in each V composition. Each linear correlation is determined by 18 data (9 slip-planes with 2 structures), except for $Ni_{63.7}V_{36.3}$ composition that has 108 data (9 slip-planes with 12 structures). As the solute concentration changes, there is a variation of change rate in γ_{isf} along $\Delta\bar{\alpha}_{sum}^{1NN,isf}$ that can be achieved during slip motion. Thus, we take the linear derivative between γ_{isf} and $\Delta\bar{\alpha}_{sum}^{1NN,isf}$ in each composition in Fig. D1b. This is similar to the CRSS variation in different V compositions. For a fixed composition, the negatively large SRO variation dictates the maximum CRSS, while the largest magnitude of SRO variation in different solute compositions may significantly differ from each other.

Appendix E: Comparison with Varvenne et al. theory

The investigations into the solute effect are underpinned by inherent assumptions pertaining to elastic anisotropy and the treatment of dislocation core-widths based on semi-empiricism. In this sense, a comprehensive understanding of its relative contribution to the lattice resistance is needed. For $Ni_{63}V_{37}$ alloy composition, as an example, we employ Varvenne et al. (2016), Yin et al. (2020b) model. The main equation is given below.

$$CRSS_{Varv} = A_\tau \left(\frac{\Gamma}{b_F^3}\right)^{-\frac{1}{3}} \left(\mu_{avg}^V \frac{1+\nu_{avg}^V}{1-\nu_{avg}^V}\right)^{\frac{4}{3}} \left(\frac{\sum c_n \Delta\overline{V}_n^2}{b_F^6}\right)^{\frac{2}{3}} \tag{E1}$$

where $\mu_{avg}^V = \frac{C_{11}-C_{12}+3C_{44}}{5}$ and $\nu_{avg}^V = \frac{3B-2\mu_{avg}^V}{2(3B+\mu_{avg}^V)}$ the Voigt average of shear moduli and Poisson's ratio, $B = \frac{C_{11}+2C_{12}}{3}$ the bulk modulus, b_F the magnitude of full Burgers vector, $A_\tau = 0.01785$ the pre-factor, $\Gamma = \alpha\mu_{110/111}b_F^2$ the line tension energy, $\alpha = 0.125$ the line tension parameter, $\mu_{110/111} = \frac{C_{11}-C_{12}+C_{44}}{3}$ the shear modulus in {111} plane in ⟨110⟩ direction, c_n the composition of constituent elements, and $\Delta\overline{V}_n$ the misfit volume parameter, which is defined as below.

$$\Delta\overline{V}_n = \frac{\partial V_{alloy}}{\partial c_n} - \sum_{m=1}^{N} c_m \frac{\partial V_{alloy}}{\partial c_m} \quad \text{(E2)} \tag{E2}$$

where $V_{alloy} = V_{alloy}(c_1, c_2, \ldots, c_{N-1})$ and $\frac{\partial V_{alloy}}{\partial c_N} = 0$ in which compositions are known for a given alloy and the change in volume with concentration are calculated from the DFT (in Fig. 8a). Then, $V_{alloy} = 13.35 - 2.681c_{Ni}$, $\Delta\overline{V}_{Ni} = -0.9731$, and $\Delta\overline{V}_V = +1.7079$ at $Ni_{63.7}V_{36.3}$. Using the elastic constants in Fig. 8b and Table 1, μ_{avg}^V and ν_{avg}^V are determined as 90.87 GPa and 0.3083, respectively. This procedure results in $CRSS_{Varv} = 249.0$ MPa at 0 K. For finite temperature, the thermal activation corrections are described in the following equations,

$$CRSS_{Varv}(T,\dot{\varepsilon}) = CRSS_{Varv}\left[1-\left(\frac{kT}{\Delta E_b}\ln\frac{\dot{\varepsilon}_0}{\dot{\varepsilon}}\right)^{\frac{2}{3}}\right] \tag{E3}$$

where $\dot{\varepsilon}_0 = 10^4\ s^{-1}$ is reference strain-rate, $\dot{\varepsilon} = 10^{-3}\ s^{-1}$ the same strain-rate used in the current experiment, and ΔE_b the energy barrier for thermal activation which is defined as,

$$\Delta E_b = A_E\left(\frac{\Gamma}{b_F^2}\right)^{\frac{1}{3}} b_F^3\left(\mu_{avg}^V\frac{1+\nu_{avg}^V}{1-\nu_{avg}^V}\right)^{\frac{2}{3}}\left(\frac{\sum c_n\Delta\overline{V}_n^2}{b_F^6}\right)^{\frac{1}{3}} \tag{E4}$$

where the pre-factor A_E is 1.5618. Based on the thermal activation corrections, $CRSS_{Varv}$ at LT and RT are calculated as 213.8 MPa and 161.9 MPa. These results indicate higher CRSS than the current theory (162 MPa at LT, 97 MPa at RT) or experiments (152 MPa at LT, 102 MPa at RT). Therefore, the Varvenne model overestimates the CRSS. These are summarized in Table E1.

Table E1
Comparison of CRSS by Varvenne et al., the proposed theory (MCS) in this work, and the experiment for $Ni_{63}V_{37}$ alloy.

CRSS by	0 K	77 K	298 K
$CRSS_{Varv}$ (Eq. (E3))	249 MPa	214 MPa	162 MPa
$CRSS_{MCS}$ (This study, Eq. (18))	215 MPa	162 MPa	97 MPa
Expt. (This study)	–	152 MPa	102 MPa

The Varvenne model considers an edge dislocation and has a number of semi-empirical constants. For example, the core-width of partials are assumed as $\xi/b_F = 1.5$ (or $\xi/b_p = 2.6$), and the SFW, d, is assumed as $d/b_F \gg 7$ (or $d/b_p \gg 12.1$), which is valid for only low SFE materials. The NiV is a high SFE material. As shown in Fig. 10, $Ni_{63}V_{37}$ has core-width (ξ/b_p) ~2.0 and SFW (d/b_p) is less than ~2.0 for the compositions studied. So, the Varvenne et al. assumptions cannot capture the materials considered in this study. Finally, the Varvenne et al. theory is valid for ideally random configuration of material and was not intended for SRO configuration. We provide a comparison of the models for further insight (Table E1) but our intention is not to depreciate the role of other models.

Appendix F: Correlation with larger nearest neighbor shells

We are considering the first NN shell (1NN) in calculation in Fig. 6a. We attribute the CRSS to the SRO change over the WS cell which corresponds to the first shell in our model. Indeed, this definition is consistent with the misfit energy calculation across atom pairs above and below the slip-plane over the WS cell arrangement of atoms. In fact, our main contribution is that misfit energy calculation that does not recognize the WS cell is erroneous which is the entire body of models in the literature. The $\Delta\alpha$ defined over the WS cell lattice will not go to zero. But, defining $\Delta\alpha$ beyond the first shell to a large cell limit poses an inconsistency with the misfit-energy calculation.

First, we note that, for each atomistic configuration, the SFEs (such as γ_{us} and γ_{isf}) and elastic properties are calculated by DFT. These are independent computations from the SRO calculation. Our goal is to find the order parameter that correlates best with the properties. In this section, we show how the correlation changes by including up-to 3NN in the SRO parameters below in Fig. F1. Fig. F1a includes only the first shell "SRO change" ($\Delta\overline{\alpha}_{sum}^{1NN,isf}$), which is the same picture in Fig. 6b for comparison. Fig. F1b include both the second (2NN) and third shell (3NN) "SRO changes", namely $\Delta\overline{\alpha}_{sum}^{upto\ 3NN,isf}$, defined as below for the normalization,

$$\Delta\overline{\alpha}_{sum}^{upto\ m,isf} = \frac{1}{\sum_m Z_m}\sum_m Z_m\Delta\overline{\alpha}_{sum}^{m,isf} \tag{F1}$$

where Z_m is coordination number. For instance, $Z_{1NN} = 12$, $Z_{2NN} = 6$, and $Z_{3NN} = 24$. The weighted parameter by the coordination number is derived from Cohen-Fine formula which is in the Eq. (23). In other words, $\Delta\overline{\alpha}_{sum}^{upto1NN,isf} = \frac{1}{12}\times 12\times\Delta\overline{\alpha}_{sum}^{1NN,isf}$, and $\Delta\overline{\alpha}_{sum}^{upto3NN,isf} = \frac{1}{12+6+24}\times(12\times\Delta\overline{\alpha}_{sum}^{1NN,isf} + 6\times\Delta\overline{\alpha}_{sum}^{2NN,isf} + 24\times\Delta\overline{\alpha}_{sum}^{3NN,isf})$. As shown in Fig. F1, including higher order shell parameters does not improve the correlation between itself and properties (CRSS, γ_{isf}), and in fact has a negative impact on the correlation (Fig. F1b). Also, in order to convey the correlation quantitatively, we plot absolute Pearson's correlation coefficient between γ_{isf} and each $\Delta\alpha$ parameter in Fig. F1c and d. Pearson's correlation coefficient is defined as below (Pilania et al., 2013; You et al., 2019, 2022),

$$r_i = \frac{\sum_{k=1}^n\left(x_{i,k}-\overline{x}_i\right)\left(y_{i,k}-\overline{y}_i\right)}{\sqrt{\sum_{k=1}^n\left(x_{i,k}-\overline{x}_i\right)^2}\sqrt{\sum_{k=1}^n\left(y_{i,k}-\overline{y}_i\right)^2}} \tag{F2}$$

where x_i is order parameter (such as $\Delta\overline{\alpha}_{sum}^{1NN,isf}$, $\Delta\overline{\alpha}_{sum}^{2NN,isf}$, $\Delta\overline{\alpha}_{sum}^{3NN,isf}$, $\Delta\overline{\alpha}_{sum}^{upto2NN,isf}$, and $\Delta\overline{\alpha}_{sum}^{upto3NN,isf}$), y_i is output to compare (γ_{isf}), and k stands for each data point of the total $n = 108$ slip-planes. As shown in Fig. F1c and d, including higher order parameters does not improve the correlation to the properties.

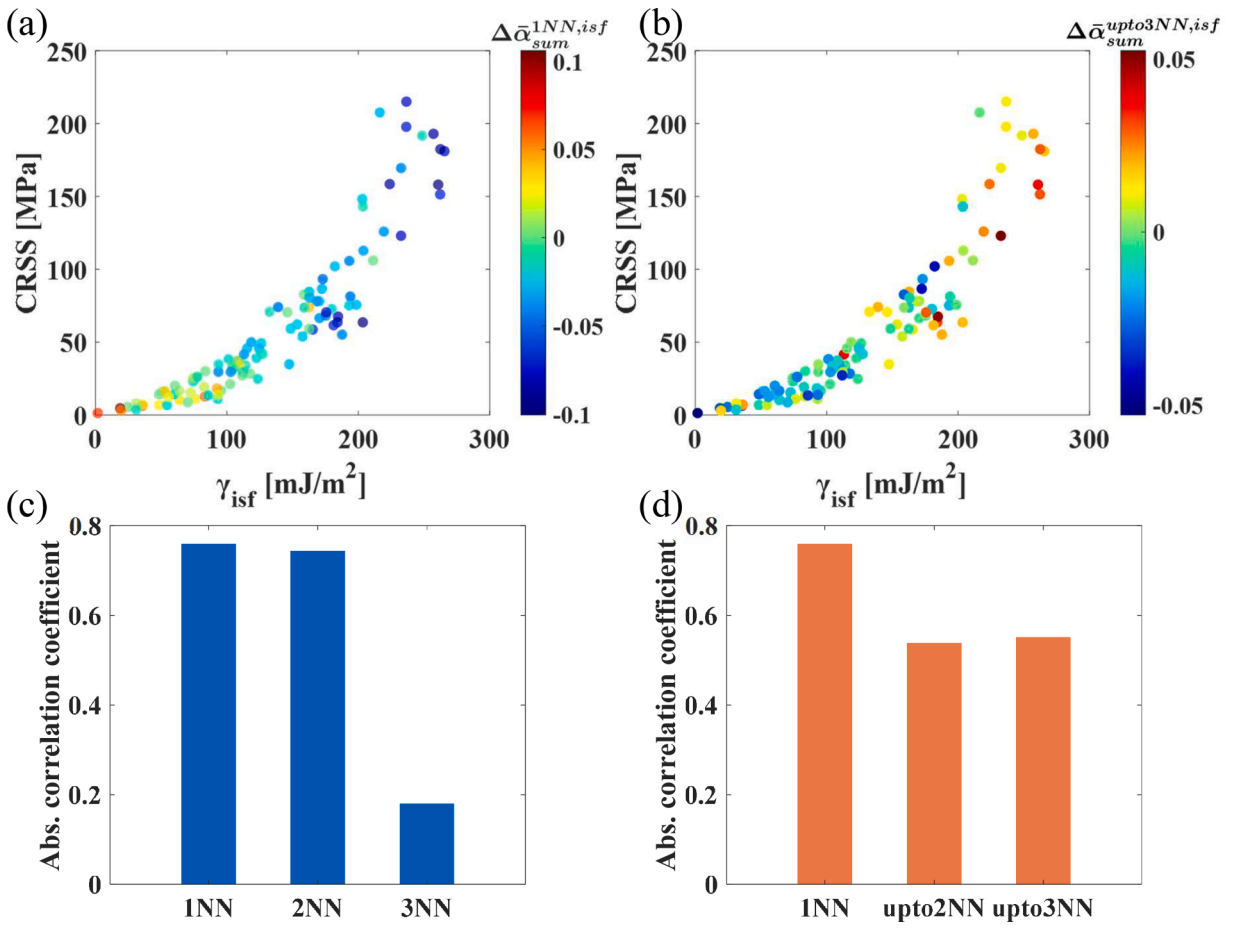

Fig. F1. Correlation analysis of higher SRO parameters: CRSS variation for intrinsic stacking fault energy (γ_{isf}) and (a) $\Delta\bar{\alpha}_{sum}^{1NN,u_{(112)}}$ or (b) $\Delta\bar{\alpha}_{sum}^{upto\ 3NN,isf}$, summed up-to 3NN shell at ISF point for $Ni_{63.7}V_{36.3}$ alloy; Absolute Pearson's correlation coefficients between γ_{isf} and each $\Delta\alpha$ parameter for (c) individual m-th shell "SRO change", $\Delta\bar{\alpha}_{sum}^{m,isf}$, and (d) including all "SRO changes" up-to m-th shell, $\Delta\bar{\alpha}_{sum}^{upto\ m,isf}$.

References

Abuzaid, W., Sehitoglu, H., 2017. Critical resolved shear stress for slip and twin nucleation in single crystalline FeNiCoCrMn high entropy alloy. Mater. Charact. 129, 288–299.

Argon, A., 2007. Strengthening Mechanisms in Crystal Plasticity. Oxford University Press.

Barnett, D.M., Lothe, J., 1974. An image force theorem for dislocations in anisotropic bicrystals. J. Phys. F Met. Phys. 4, 1618–1635.

Celebi, O.K., Mohammed, A.S.K., Krogstad, J.A., Sehitoglu, H., 2022. Evolving dislocation cores at twin boundaries: theory of CRSS elevation. Int. J. Plast. 148, 103141.

Celebi, O.K., Mohammed, A.S.K., Sehitoglu, H., 2023. Effect of dislocation character on the CRSS. Acta Mater. 254, 118982.

Chen, S., Aitken, Z.H., Pattamatta, S., Wu, Z., Yu, Z.G., Srolovitz, D.J., Liaw, P.K., Zhang, Y.W., 2021a. Simultaneously enhancing the ultimate strength and ductility of high-entropy alloys via short-range ordering. Nat. Commun. 12, 4953.

Chen, X., Wang, Q., Cheng, Z., Zhu, M., Zhou, H., Jiang, P., Zhou, L., Xue, Q., Yuan, F., Zhu, J., Wu, X., Ma, E., 2021b. Direct observation of chemical short-range order in a medium-entropy alloy. Nature 592, 712–716.

Chowdhury, P., Sehitoglu, H., Abuzaid, W., Maier, H.J., 2015. Mechanical response of low stacking fault energy Co–Ni alloys – Continuum, mesoscopic and atomic level treatments. Int. J. Plast. 71, 32–61.

Cohen, J.B., Fine, M.E., 1962. Some aspects of short-range order. J. Phys. Radium 23, 749–762.

Cowley, J.M., 1960. Short- and long-range order parameters in disordered solid solutions. Phys. Rev. 120, 1648–1657.

Ding, J., Yu, Q., Asta, M., Ritchie, R.O., 2018. Tunable stacking fault energies by tailoring local chemical order in CrCoNi medium-entropy alloys. In: , 115, pp. 8919–8924.

Ferrari, A., Körmann, F., Asta, M., Neugebauer, J., 2023. Simulating short-range order in compositionally complex materials. Nat. Comput. Sci. 3, 221–229.

Hastings, W.K., 1970. Monte Carlo sampling methods using Markov chains and their applications. Biometrika 57, 97–109.

Hoover, W.G., 1985. Canonical dynamics: equilibrium phase-space distributions. Phys. Rev. A 31, 1695–1697.

Joós, B., Duesbery, M.S., 1997. The peierls stress of dislocations: an analytic formula. Phys. Rev. Lett. 78, 266–269.

Kibey, S., Liu, J.B., Curtis, M.J., Johnson, D.D., Sehitoglu, H., 2006. Effect of nitrogen on generalized stacking fault energy and stacking fault widths in high nitrogen steels. Acta Mater. 54, 2991–3001.

Kioussis, N., Herbranson, M., Collins, E., Eberhart, M.E., 2002. Topology of electronic charge density and energetics of planar faults in FCC metals. Phys. Rev. Lett. 88, 125501.
Kostiuchenko, T., Ruban, A.V., Neugebauer, J., Shapeev, A., Körmann, F., 2020. Short-range order in face-centered cubic VCoNi alloys. Phys. Rev. Mater. 4, 113802.
Kresse, G., Furthmüller, J., 1996. Efficient iterative schemes for ab initio total-energy calculations using a plane-wave basis set. Phys. Rev. B 54, 11169–11186.
Kresse, G., Joubert, D., 1999. From ultrasoft pseudopotentials to the projector augmented-wave method. Phys. Rev. B 59, 1758–1775.
Lennard-Jones, J.E., 1931. Cohesion. Proc. Phys. Soc. 43, 461.
Li, Q.J., Sheng, H., Ma, E., 2019. Strengthening in multi-principal element alloys with local-chemical-order roughened dislocation pathways. Nat. Commun. 10, 3563.
Liu, G.D., Luo, X.M., Zou, J.P., Zhang, B., Zhang, G.P., 2023. Ultrahigh grain boundary strengthening ability of VCoNi medium entropy alloy. Mater. Charact. 206, 113419.
Mohammed, A.S.K., Celebi, O.K., Sehitoglu, H., 2022. Critical stress prediction upon accurate dislocation core description. Acta Mater. 233, 117989.
Nabarro, F.R.N., 1947. Dislocations in a simple cubic lattice. Proc. Phys. Soc. 59, 256–272.
Niu, C., LaRosa, C.R., Miao, J., Mills, M.J., Ghazisaeidi, M., 2018. Magnetically-driven phase transformation strengthening in high entropy alloys. Nat. Commun. 9, 1363.
Norman, N., Warren, B.E., 2004. X-Ray Measurement of short range order in Ag-Au. J. Appl. Phys. 22, 483–486.
Nosé, S., 1984. A unified formulation of the constant temperature molecular dynamics methods. J. Chem. Phys. 81, 511–519.
Oh, H.S., Kim, S.J., Odbadrakh, K., Ryu, W.H., Yoon, K.N., Mu, S., Körmann, F., Ikeda, Y., Tasan, C.C., Raabe, D., Egami, T., Park, E.S., 2019. Engineering atomic-level complexity in high-entropy and complex concentrated alloys. Nat. Commun. 10, 2090.
Peierls, R., 1940. The size of a dislocation. Proc. Phys. Soc. 52, 34.
Perdew, J.P., Burke, K., Ernzerhof, M., 1996. Generalized gradient approximation made simple. Phys. Rev. Lett. 77, 3865–3868.
Picak, S., Singh, P., Salas, D., Tunes, M.A., Fang, X., Zhou, L., Kramer, M.J., Chumlyakov, Y.I., Johnson, D.D., Arroyave, R., Ren, Y., Karaman, I., 2023. Orientation dependence of the effect of short-range ordering on the plastic deformation of a medium entropy alloy. Mater. Sci. Eng. A 888, 145309.
Pilania, G., Wang, C., Jiang, X., Rajasekaran, S., Ramprasad, R., 2013. Accelerating materials property predictions using machine learning. Sci. Rep. 3, 2810.
Qi, Y., Mishra, R.K., 2007. Ab initio study of the effect of solute atoms on the stacking fault energy in aluminum. Phys. Rev. B 75, 224105.
Seol, J.B., Ko, W.S., Sohn, S.S., Na, M.Y., Chang, H.J., Heo, Y.U., Kim, J.G., Sung, H., Li, Z., Pereloma, E., Kim, H.S., 2022. Mechanically derived short-range order and its impact on the multi-principal-element alloys. Nat. Commun. 13, 6766.
Shim, J.H., Ko, W.S., Kim, K.H., Lee, H.S., Lee, Y.S., Suh, J.Y., Cho, Y.W., Lee, B.J., 2013. Prediction of hydrogen permeability in V–Al and V–Ni alloys. J. Memb. Sci. 430, 234–241.
Simmons, G., Wang, H., 1971. Single crystal elastic constants and calculated aggregate properties, 2nd ed. M.I.T. Press, Cambridge, MA.
Singh, P., Smirnov, A.V., Johnson, D.D., 2015. Atomic short-range order and incipient long-range order in high-entropy alloys. Phys. Rev. B 91, 224204.
Smith, J.F., Carlson, O.N., Nash, P.G., 1982. The Ni−V (Nickel−Vanadium) system. Bull. Alloy Ph. Diagr. 3, 342–348.
Stroh, A.N., 1958. Dislocations and cracks in anisotropic elasticity. the philosophical magazine: a. J. Theor. Exp. Appl. Phys. 3, 625–646.
Sun, S.J., Tian, Y.Z., Lin, H.R., Dong, X.G., Wang, Y.H., Wang, Z.J., Zhang, Z.F., 2019. Temperature dependence of the Hall–Petch relationship in CoCrFeMnNi high-entropy alloy. J. Alloy. Compd. 806, 992–998.
Tamm, A., Aabloo, A., Klintenberg, M., Stocks, M., Caro, A., 2015. Atomic-scale properties of Ni-based FCC ternary, and quaternary alloys. Acta Mater. 99, 307–312.
Thompson, A.P., Aktulga, H.M., Berger, R., Bolintineanu, D.S., Brown, W.M., Crozier, P.S., in 't Veld, P.J., Kohlmeyer, A., Moore, S.G., Nguyen, T.D., Shan, R., Stevens, M.J., Tranchida, J., Trott, C., Plimpton, S.J., 2022. LAMMPS - a flexible simulation tool for particle-based materials modeling at the atomic, meso, and continuum scales. Comput. Phys. Commun. 271, 108171.
van de Walle, A., Tiwary, P., de Jong, M., Olmsted, D.L., Asta, M., Dick, A., Shin, D., Wang, Y., Chen, L.Q., Liu, Z.K., 2013. Efficient stochastic generation of special quasirandom structures. CALPHAD 42, 13–18.
Varvenne, C., Luque, A., Curtin, W.A., 2016. Theory of strengthening in fcc high entropy alloys. Acta Mater. 118, 164–176.
Vítek, V., 1968. Intrinsic stacking faults in body-centred cubic crystals. the philosophical magazine: a. J. Theor. Exp. Appl. Phys. 18, 773–786.
Walsh, F., Zhang, M., Ritchie, R.O., Minor, A.M., Asta, M., 2023. Extra electron reflections in concentrated alloys do not necessitate short-range order. Nat. Mater. 22, 926–929.
Widom, M., Huhn, W.P., Maiti, S., Steurer, W., 2014. Hybrid Monte Carlo/molecular dynamics simulation of a refractory metal high entropy alloy. Metall. Mater. Trans. A 45, 196–200.
Wu, H., Mayeshiba, T., Morgan, D., 2016. High-throughput ab-initio dilute solute diffusion database. Sci. Data 3, 160054.
Wu, Z., Bei, H., Pharr, G.M., George, E.P., 2014. Temperature dependence of the mechanical properties of equiatomic solid solution alloys with face-centered cubic crystal structures. Acta Mater. 81, 428–441.
Yin, B., Maresca, F., Curtin, W.A., 2020a. Vanadium is an optimal element for strengthening in both fcc and bcc high-entropy alloys. Acta Mater. 188, 486–491.
Yin, B., Yoshida, S., Tsuji, N., Curtin, W.A., 2020b. Yield strength and misfit volumes of NiCoCr and implications for short-range-order. Nat. Commun. 11, 2507.
You, D., Celebi, O., Mohammed, A.S.K., Sehitoglu, H., 2023a. Negative stacking fault energy in FCC materials-its implications. Int. J. Plast., 103770
You, D., Celebi, O.K., Mohammed, A.S.K., Abueidda, D.W., Koric, S., Sehitoglu, H., 2023b. CRSS determination combining ab-initio framework and surrogate neural networks. Int. J. Plast., 103524
You, D., Ganorkar, S., Joo, M., Park, D., Kim, S., Kang, K., Lee, D., 2019. Ab initio study of H, B, C, N, O, and self-interstitial atoms in hcp-Zr. J. Alloy. Compd. 787, 631–637.
You, D., Zhang, H., Ganorkar, S., Kim, T., Schroers, J., Vlassak, J.J., Lee, D., 2022. Electrical resistivity as a descriptor for classification of amorphous versus crystalline phases of alloys. Acta Mater. 231, 117861.
Zhang, M., Yu, Q., Frey, C., Walsh, F., Payne, M.I., Kumar, P., Liu, D., Pollock, T.M., Asta, M.D., Ritchie, R.O., Minor, A.M., 2022. Determination of peak ordering in the CrCoNi medium-entropy alloy via nanoindentation. Acta Mater. 241, 118380.
Zhang, R., Zhao, S., Ding, J., Chong, Y., Jia, T., Ophus, C., Asta, M., Ritchie, R.O., Minor, A.M., 2020. Short-range order and its impact on the CrCoNi medium-entropy alloy. Nature 581, 283–287.
Zhang, R., Zhao, S., Ophus, C., Deng, Y., Vachhani, S.J., Ozdol, B., Traylor, R., Bustillo, K.C., Morris, J.W., Chrzan, D.C., Asta, M., Minor, A.M., 2019. Direct imaging of short-range order and its impact on deformation in Ti-6Al. Sci. Adv. 5, eaax2799.
Zhao, S., Osetsky, Y., Stocks, G.M., Zhang, Y., 2019. Local-environment dependence of stacking fault energies in concentrated solid-solution alloys. NPJ Comput. Mater. 5, 13.
Zhao, S., Stocks, G.M., Zhang, Y., 2017. Stacking fault energies of face-centered cubic concentrated solid solution alloys. Acta Mater. 134, 334–345.
Zhou, L., Wang, Q., Wang, J., Chen, X., Jiang, P., Zhou, H., Yuan, F., Wu, X., Cheng, Z., Ma, E., 2022. Atomic-scale evidence of chemical short-range order in CrCoNi medium-entropy alloy. Acta Mater. 224, 117490.
Ziehl, T.J., Morris, D., Zhang, P., 2023. Detection and impact of short-range order in medium/high-entropy alloys. iScience 26.